Remote Sensing of Environment 222 (2019) 34–49

Contents lists available at ScienceDirect

Remote Sensing of Environment

journal homepage: www.elsevier.com/locate/rse

# Watershed-scale mapping of fractional snow cover under conifer forest canopy using lidar

Tihomir S. Kostadinov[a,*,1], Rina Schumer[b], Mark Hausner[b], Kat J. Bormann[c], Rowan Gaffney[d], Kenneth McGwire[e], Thomas H. Painter[c], Scott Tyler[d], Adrian A. Harpold[f]

[a] Department of Liberal Studies, California State University San Marcos, San Marcos, CA, USA
[b] Division of Hydrologic Sciences, Desert Research Institute, Reno, NV, USA
[c] Jet Propulsion Laboratory, California Institute of Technology, Pasadena, CA, USA
[d] Dept. of Geological Sciences and Engineering, University of Nevada, Reno, NV, USA
[e] Division of Earth and Ecosystem Sciences, Desert Research Institute, Reno, NV, USA
[f] Department of Natural Resources and Environmental Science, University of Nevada, Reno, NV, USA

ARTICLE INFO

*Keywords:*
Fractional snow cover
Snow disappearance
Snow ablation
Conifer forests
Mountain forests
Lidar
Distributed temperature sensing
Snow-vegetation interactions
Canopy correction for fSCA
Sagehen experimental watershed
Sierra Nevada

ABSTRACT

The distribution of snow cover is critical for predicting ecohydrological processes and underpins mountain water supplies in ranges like the Sierra Nevada in the Western United States. Many key water supply areas are covered by montane forests, which have substantial effects on the amount and timing of snowmelt. In-situ observations of snow-forest interactions have limited spatial coverage and remote sensing using optical sensors (e.g. MODIS) cannot observe snow cover below the canopy. In this study, we developed and verified a lidar-based method to detect snow cover under canopy, investigated how fractional snow covered area (fSCA) varies with topography in open versus under canopy areas and developed a correction factor that could be used to improve satellite-derived fSCA products. We developed our new method using three snow-on lidar overflights and verified it with in-situ distributed temperature sensor (DTS) observations at Sagehen Creek watershed in the Sierra Nevada, California, USA. DTS validation of lidar classifications showed excellent agreement at 85–96%, including high agreement and large number of returns in under canopy locations. The lidar-derived fSCA observations generally showed earlier snow disappearance under the canopy than in open positions, which is consistent with relatively warm temperatures and greater longwave radiation. However, in contrast to expectations, areas with high solar exposure (i.e. high southwestness) exhibited higher fSCA under the canopy. Results indicated that the $k$ factor (the ratio of under canopy fSCA to open fSCA) varied systematically with southwestness and elevation. Using this factor to correct the study domain fSCA indicated that the typical assumption that $k = 1$ could lead to an up to ~0.05 bias (in fSCA units) towards overestimation. However, within 10 and 100-m individual pixels the fSCA overprediction bias can be 25–30% for higher fSCA values. Although uncertainty would be reduced using higher snow-on lidar point densities, our method shows promise to improve the typical assumption that snow disappearance is identical in under the canopy and in the open ($k = 1$). Future applications of our lidar-based method at different sites with varying climate, topography and vegetation structure has the dual potential to expand understanding of snow-forest interactions in complex terrain and improve operational fSCA products.

## 1. Introduction

Melt of seasonal snowpacks from mountain forests are critical for water resources in the Northern Hemisphere (Barnett and Adam, 2005; NRC, 2008). In Mediterranean mountain climates characterized by wet winters and dry summers, such as the mountainous Western United States, annual runoff is dominated by snow melt (Serreze et al., 1999; Li et al., 2017). Consequently, changes to snowmelt and shifts from rain to snow have important implications for streamflow (Berghuijs et al., 2014; Barnhart et al., 2016) and land surface albedo (Robock, 1984; Berg and Hall, 2017). Conifer forests occupy much of the snow zone in the Western USA and exert strong controls on snow mass and energy budgets. Changes to forest canopy from natural and anthropogenic disturbances can alter snow processes that drive streamflow generation

* Corresponding author.
*E-mail address:* tkostadinov@csusm.edu (T.S. Kostadinov).
[1] Previously at Division of Hydrologic Sciences, Desert Research Institute, Reno, NV, USA.

https://doi.org/10.1016/j.rse.2018.11.037
Received 27 April 2018; Received in revised form 22 November 2018; Accepted 24 November 2018
Available online 22 December 2018

(Biederman et al., 2015; Buma and Livneh, 2015). For example, there is evidence of both increasing and decreasing snow accumulation following disturbance from mountain pine beetles (e.g. Pugh and Small, 2012; Biederman et al., 2014). Observing snow-forest interactions is critical to managing water availability for local ecosystem and downstream needs. However, the complex interactions of forest canopy and snow are challenging to characterize because they are dynamic in space and time.

Conifer forests exert counteracting biophysical controls on snow. On one hand, denser forest canopy generally reduces snow accumulation by intercepting incoming snowfall (Hedstrom and Pomeroy, 1998; Storck et al., 2002; Moeser et al., 2016). On the other hand, forest canopy has complex effects on snow ablation (i.e. snow mass loss from melt, sublimation, and evaporation) by both shading the snowpack from shortwave energy inputs (Essery et al., 2008; Veatch et al., 2009) and reducing turbulent kinetic energy (Link and Marks, 1999; Marks et al., 2008), while also emitting longwave radiation to the snowpack more effectively than the atmosphere (Sicart et al., 2006; Pomeroy et al., 2009). Forests also alter patterns of wind-driven snow redistribution and preferential accumulation (e.g. Marks et al., 2002; Cristea et al., 2017). The interplay of seasonally varying shortwave and longwave energy and interception lead to differential snow disapearance in open versus under canopy locations (Veatch et al., 2009; Musselman et al., 2012; Lundquist et al., 2013; Broxton et al., 2014; Coons et al., 2014; Harpold et al., 2014; Dickerson-Lange et al., 2015). Lundquist et al. (2013) developed a conceptual model to argue that sites with December–February (DJF) temperatures warmer than $-1\,^{\circ}C$ were likely to retain snow longer in the open than under canopy locations, while colder sites retain snow in under canopy locations longer. This differential response to canopy is driven by tradeoffs between forests limiting shortwave radiation inputs and emitting longwave radiation, both of which are sensitive to latitude, climate and forest structure (Lundquist et al., 2013). The differential snow disappearance between open and under canopy locations has implications for ecohydrological processes, like root distribution and tree water stress (Small and McConnell, 2008), and challenges conventional large-scale snow observation and modeling techniques.

Observing snow under forest canopy is challenging with either in-situ or remote observations due to logistical constraints and the highly dynamic timing of snow disappearance in forests. Inexpensive temperature loggers are routinely used to detect the presence or absence of snow by exploiting its insulating properties (Lundquist and Lott, 2008; Raleigh et al., 2013). Cameras offer more spatial resolution than point measurements but are difficult to automate and spatially register (Dickerson-Lange et al., 2015; Garvelmann et al., 2013). Distributed temperature sensing (DTS) measurements along a fiber optic cable (Tyler et al., 2008; Tyler et al., 2009) greatly expand the spatial and temporal resolution, but are somewhat limited in spatial coverage and challenging to install and operate (Lutz et al., 2012; Dickerson-Lange et al., 2015). While these field observations have strengths and weaknesses, they cannot match the spatial coverage offered by remote sensing techniques. However, remote sensing observations of snow are challenging because the forest canopy occludes optical retrievals (Rittger et al., 2013), and also interferes with thermal (Lundquist et al., 2018) and microwave-based sensing (e.g. Pulliainen et al., 1999; Royer et al., 2010). Airplane and terrestrial-based lidar measure snowpack extent at ~1 m scales and decimeter accuracy (Harpold et al., 2015a). Because lidar emits an active energy source (e.g. 532–1550 nm) that can penetrate forest canopy, lidar observations have been successfully used to simultaneously observe snowpack depth and forest structure (Deems et al., 2013; Harpold et al., 2014; Harpold et al., 2015a). However, lidar's ability and accuracy for estimating under-canopy snow cover has received little attention (Zheng et al., 2016).

Several optical remote sensing retrieval techniques can be used to detect snow presence or absence and estimate fractional snow cover area (fSCA), but make assumptions about under canopy snow cover. Optical sensors take advantage of strong differences in spectral properties of snow versus vegetation, and rock/soil (Hall and Riggs, 2007; Painter et al., 2009). These strong spectral contrasts also allow snow to be classified from an RGB camera (Garvelmann et al., 2013). However, without improved information on snow-forest interactions, conventional optical remote sensing products need to make assumptions about snow cover under forest canopy that are not directly observed. From a point-scale perspective, snow is observed as either present or absent. As the spatial scale increases, however the pixel can become a mix of snow and non-snow and can have fSCA between 0 and 1 (0% and 100%). Snow disappearance timing is therefore related to fSCA, i.e. snow is disappearing as fSCA decreases, but fSCA cannot explicitly account for the disappearance of snow because of mixed pixel effects. Remote sensing derived fSCA is a fundamental long-term observation (Dozier and Painter, 2004; Painter et al., 2009) and critical to the development of many current snowmelt models (e.g. Carroll et al., 2001; Molotch and Margulis, 2008; Musselman et al., 2012), as well as SWE reconstruction models (e.g. Kahl, 2013; Bair et al., 2016). fSCA is routinely retrieved using multi- and hyper-spectral platforms using their respective spectral mixture analysis algorithms, i.e. MEMSCAG (Painter et al., 2003), MODSCAG and TMSCAG (Painter et al., 2009). There is potential to develop higher temporal resolution fSCA from geostationary satellites like GOES (i.e. GOESRSCAG (Cline et al., 2010)) or higher spatial resolution fSCA without view angle effects from satellites like Sentinel-2 and similar future missions (ESA, 2018). In all of these platforms, the tree canopy occludes snow cover and generally requires the assumption that the fSCA under the canopy is the same as the fSCA of the viewable pixel fraction (e.g. Molotch and Margulis, 2008; Rittger et al., 2013; Raleigh et al., 2013) or similar assumptions. For example, the current implementation of the MODSCAG algorithm (Painter et al., 2009) assumes that if the viewable fSCA is greater than zero and the other coverage in the pixel is vegetation, then fSCA is assumed to be 100% below the canopy. Metsämäki et al. (2012) do not rely on such assumptions and instead develop models that explicitly take into account forest transmissivity in their *SCAmod* method (Metsämäki et al., 2012). More information about under canopy fSCA has the potential to relax assumptions about under canopy snow cover in operational products, improve the accuracy of current snowmelt models (Slater et al., 2013) and take advantage of higher resolution fSCA products in the future.

In this paper, we developed a new method to estimate fSCA under forest canopy over large spatial extents using lidar with the dual motivations of characterizing snow-vegetation interactions and improving operational fSCA estimates. Our method is the first application of lidar that takes advantage of its ability to penetrate the forest canopy in order to explicitly map under canopy snow cover. We used a unique set of multi-temporal lidar datasets and large-scale DTS field observations from a heavily forested watershed in the Sierra Nevada range to estimate fSCA separately in open areas versus under canopy, and develop our new lidar-based method. Specifically, we addressed the following questions:

1) ***can fSCA be reliably estimated under conifer tree canopies with lidar-derived snow depth,***
2) ***how does the relationship between open-area fSCA and under-canopy fSCA vary based on slope/aspect and elevation, and***
3) ***can a spatially variable fSCA correction factor elucidate controls on under-canopy snow processes and help correct coarser remote sensing retrievals?***

Lidar observations were used to derive differences between under canopy and open fSCA by taking advantage of the high point density of lidar at watershed scales to make new inferences about snow-vegetation interactions and biases in current satellite-based fSCA estimates in montane forests.

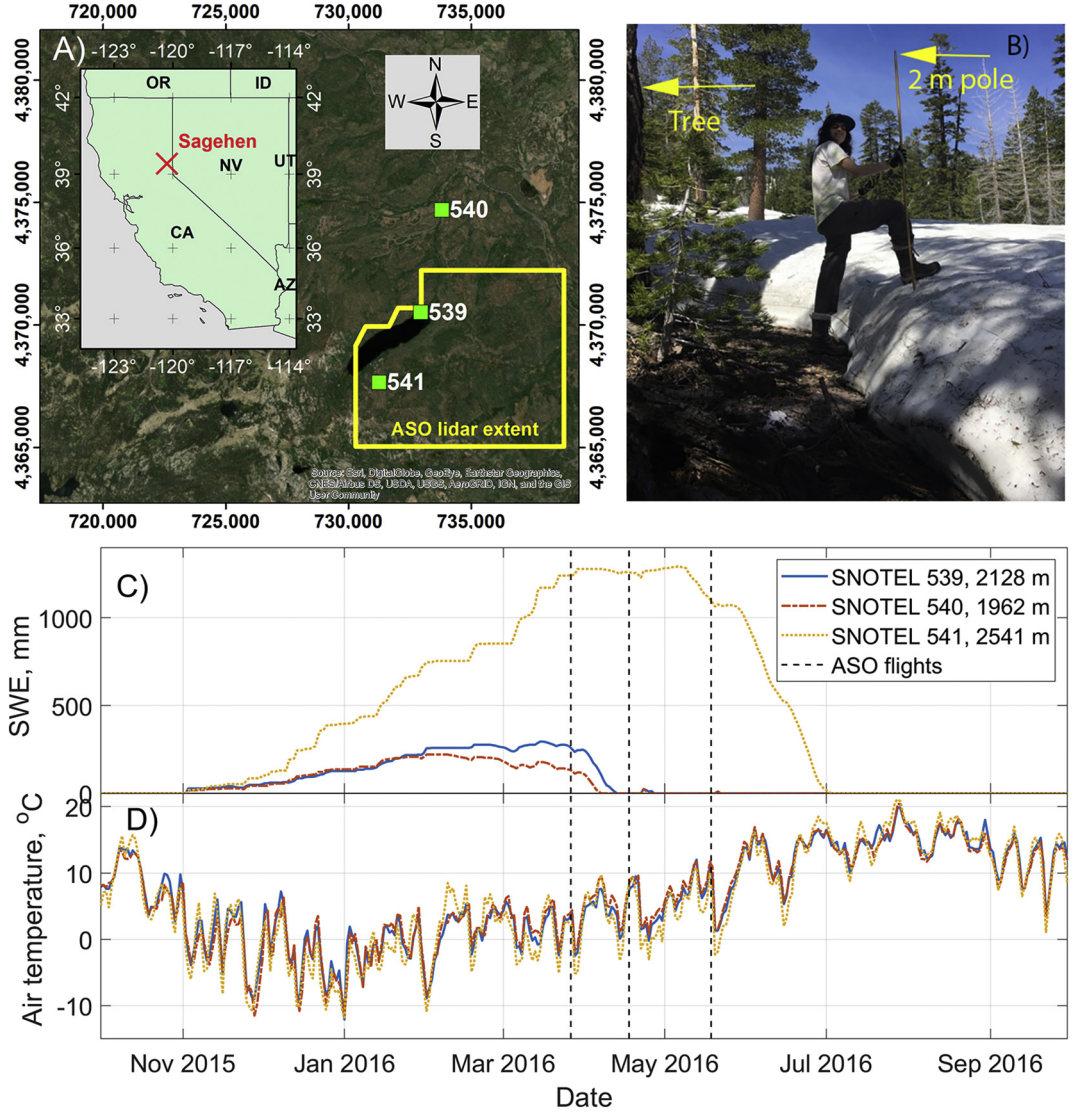


**Fig. 1.** A) Location of the Sagehen Experimental Watershed within the Southwestern USA. SNOTEL station locations are shown as a green square with the SNOTEL station number indicated. The spatial extent of the snow on ASO lidar coverage used in this analysis is shown in yellow. B) An example of snow ablation near canopies illustrating the dramatic potential difference between open and under-canopy snow dynamics. Photograph taken within the study domain on May 18, 2016 (day of third lidar flight) at 39°25′20″N, 120°18′1.5″W, 2370 m elevation above sea level, by A. Harpold. C) Time series of snow water equivalent (mm) for water year 2016 at three SNOTEL stations (see legend), located in or near the Sagehen Experimental watershed in the Northern Sierra Nevada range of California, USA. The station elevations in meters are indicated in the legend, and the station locations are shown on the map in panel A. The dates of the three ASO flights are indicated with vertical black dashed lines; D) Daily average air temperatures at the same three SNOTEL stations. (For interpretation of the references to colour in this figure legend, the reader is referred to the web version of this article.)

## 2. Data and methods

### 2.1. Study site

The study site encompassed an approximately 8 km by 7 km region covering the Sagehen Experimental Watershed (henceforth referred to as Sagehen) and surrounding areas. Sagehen is a forested mountainous watershed located in the Northern Sierra Nevada of California just east of the Sierra crest (Fig. 1A). Characteristics of Sagehen are given in Fig. 2, which also displays the DTS cable layout. For reference, the location marked as 0 m along the DTS cable in Fig. 2 panels is at 39°25′53.46″N, 120°14′23.14″W (WGS84). Elevations in the study area ranged from ~1800 m to ~2700 m above sea level (with respect to the NAVD88 datum) and were split into bins as shown in Fig. 2A. Independence Lake (Fig. 2A) and a few small ponds fall within this area and were excluded from the analysis. Sagehen is mostly covered by conifer forests of different density, ranging from 0% to 100% tall canopy at the 10 m scale (Fig. 2C). Snow water equivalent (SWE) and average daily air temperature data from SNOTEL (Serreze et al., 1999) stations # 539, 540, and 541 were downloaded (https://www.wcc.nrcs.usda.gov/) and used to illustrate SWE time series in 2016. Station locations are shown in Fig. 1A.

In order to quantify the effects of varying energy budgets/radiation load on snow cover dynamics, the topographic index of southwestness was used. Southwestness was calculated at 1 m spatial resolution (Fig. 2B) from the NCALM lidar-derived bare earth DEM's slope and aspect (see Sect. 2.2) expressed in radians as follows:

$$Southwestness = -\cos\left(Aspect - \frac{\pi}{4}\right)\sin(Slope) \quad (1)$$

Southwestness varies from +1 on southwest-facing terrain with slope 90° (areas exposed to more solar radiation during afternoon heat), to −1 on northeast-facing terrain with slope 90°, and it is 0 for flat terrain. It is valid for the Northern Hemisphere and is similar to the

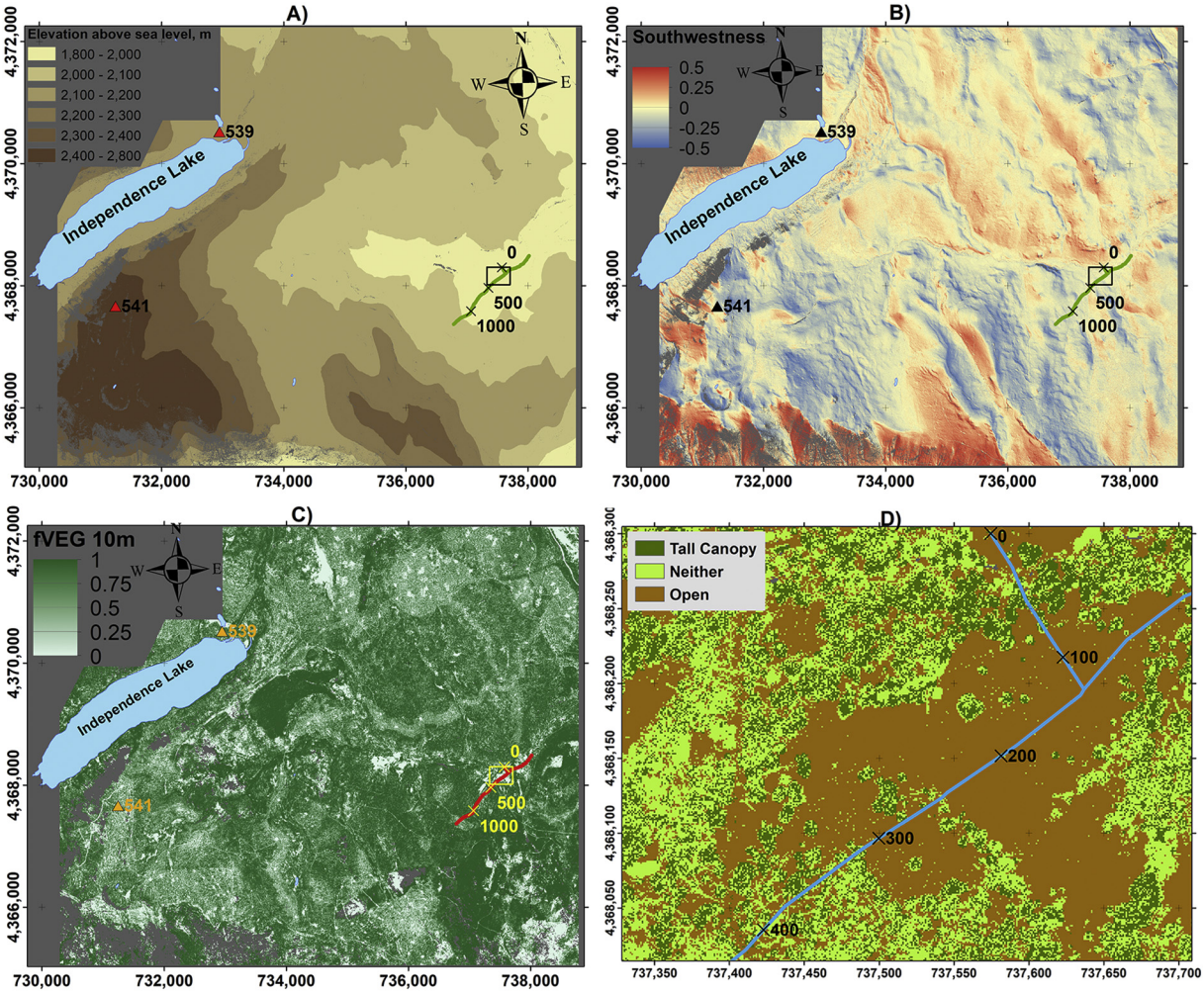


**Fig. 2.** A) Elevation map of the study area – the Sagehen Experimental Watershed and Independence Lake area in the Northern Sierra Nevada range of California, USA. Elevation bands are shown in tan/brown as used in the analysis. B) Map of southwestness (Eq. (1)) in the study area, C) map of the fraction of tall canopy, fVEG, at a 10 m resolution, derived from the NCALM 2014 snow-off lidar, D) zoomed in map of vegetation structure, classifying pixels as tall trees, open areas or neither (at 1 m resolution) (See Sect. 2.2). The zoomed in area is indicated with a black rectangle in panels A and B and a yellow rectangle in panel C. The SNOTEL station locations are shown as triangles in panels A–C (numbers indicating station designations). The DTS cable layout is indicated in light green in panels A–B, red in C, and light blue in D, and distance in meters along the cable is indicated with crosses. Missing data are shown as dark grey. The maps' projection for these and subsequent maps is UTM Zone 10 N, datum NAD83. (For interpretation of the references to colour in this figure legend, the reader is referred to the web version of this article.)

diurnal anisotropic heating index (DAH) (Böhner and Antonić, 2009); it represents snow ablation effects in the Sierra Nevada better than more complex radiation/heat load indices (Cristea et al., 2017). Many previous studies have used northness to quantify solar shelter (Molotch and Margulis, 2008; Veatch et al., 2009) and would have likely yielded similar results to those found here. In order to investigate the dependence of snow cover on topography, the 1 m classified ASO pixels were binned into 48 bins based on elevation and southwestness. The elevation bins in meters were as follows: < 2000, [2000, 2100), [2100, 2200), [2200, 2300), [2300, 2400), and > 2400 m and southwestness bins comprised of the following intervals: [−0.5, −0.3), [−0.3, −0.2), [−0.2, −0.1), [−0.1, 0.0), [0.0, 0.1), [0.1, 0.2), [0.2, 0.3), and [0.3, 0.5]. The fractional vegetation cover (fVEG) was computed at 10 m resolution as the fraction of 1 m pixels that comprise a 10-m pixel and had NCALM vegetation heights > 2 m (Fig. 2C).

### 2.2. Lidar data sets & processing

Two different sets of airborne lidar data were used – a snow-off data set collected in the summer of 2014, and three snow-on overflights during the snow depletion in 2016 (Fig. 1A, C–D). The 2014 snow-off dataset is part of the USFS Tahoe National Forest lidar survey collected by the National Center for Airborne Laser Mapping (NCALM) (USFS, 2015) hereafter referred to as NCALM or snow-off lidar. The NASA Airborne Snow Observatory (ASO) (Painter et al., 2016) collected snow on airborne lidar data over Sagehen on March 26, April 17, and May 18, 2016. More details on the lidar datasets and their processing are provided in the Supplement.

We preprocessed the data in two important ways: by excluding areas and improving the accuracy of the lidar-derived elevation datasets. Slopes greater than 30° and lake/pond water bodies as delineated by the National Hydrography Dataset (high resolution) (https://nhd.usgs.gov/) were excluded from the analysis. We used this slope threshold because the uncertainty in elevation increases dramatically above 30 degrees slope (Takahashi et al., 2005; Tinkham et al., 2012). In order to eliminate any vertical biases between the ASO lidar return elevations and the NCALM DEM, a point-cloud-to-point-cloud comparison was performed between the two data sets above the snow-free US Highway 89 in the NE-most corner of the study domain (Fig. 2A). Only ground-classified NCALM points were used, and all ASO returns were used for this comparison. Results indicated that the lowest 10th percentile of the ASO to NCALM differences in mean elevations in each grid cell over

Hwy 89 was 0.23 m, 0.26 m, and 0.38 m for the March 26, April 17 and May 18, 2016 ASO flights, respectively. These values were subtracted from all ASO return elevations in order to correct vertical biases relative to the NCALM DEM (cf. Ferraz et al., 2018). As explained later, these vertical biases likely resulted from a number of different error sources; we note that vertical co-registration and corrections of snow-on datasets is fairly routine (Hopkinson et al., 2012).

We developed a method to classify vegetation and snow presence in order to map snow cover in both under canopy and open locations. This method first determined whether vegetation existed above 2 m and if so, whether it had low branches below 2 m. To do this, we used the snow-off lidar point cloud data using a 1-m grid to identify returns above 2 m, deemed forest covered, and returns between 0.15 and 2 m which we interpreted as low vegetation (e.g. near ground level branches). Areas with low vegetation were completely excluded from the analysis because low branches could be confused with the snow surface. Forest covered areas without low vegetation (i.e. no snow off returns $< 2$ m and $\geq 0.15$ m) were available and used for under canopy snow cover estimation. In addition, areas with vegetation $< 0.15$ m were classified as open. After the vegetation classification, the presence or absence of snow was determined for each of the three ASO snow-on lidar datasets. Each 1-m ASO pixel that was either open or forest-covered without low vegetation was classified as snow covered if the within-pixel mean ASO return elevation was $\geq 0.15$ m and $< 2$ m for forest-covered pixels without low vegetation and $\geq 0.15$ and $\leq 5$ m for open area pixels. Conversely, a pixel was classified as snow free if ASO returns are found between $-0.30$ m and 0.15 m. Details of the classification criteria are given in Supplement Tables S1 and S2, including an example of application of the criteria used to classify a pixel. The goal of these classifications was a conservative and rigorous method for mapping snow presence under canopy that can be upscaled to fSCA estimates. Furthermore, choice of the various thresholds for pixel exclusion and vegetation and snow classification was driven by the need to compromise between greater accuracy and greater data availability. The optimum height thresholds are likely to differ in areas with dissimilar snow and vegetation characteristics. ASO lidar snow classification both in open areas and under the canopy were validated with in-situ DTS measurements, described in the following Sect. 2.3. This represents the first published ASO lidar field validation under the canopy, additional validation efforts are underway (Painter et al., 2016).

### 2.3. Distributed temperature sensing in-situ measurements

Distributed temperature sensing (DTS) uses a fiber-optic cable as a thermometer and relies on Raman spectrum scattering and time-domain reflectometry to derive near-continuous temperatures along the cable over the course of the deployment (Selker et al., 2006; Tyler et al., 2009; Hausner et al., 2011). The DTS cables were interrogated with a Silixa XT (Hertfordshire, UK) DTS instrument to return temperature observations every 0.25 m along the length of each cable. The DTS cable layout is shown in Fig. 2, with the DTS instrument located at the 0 m points. The cables were georeferenced to UTM WGS84 space using a hand-held Trimble GNSS (Sunnyvale, CA) and then converted to NAD83 using VDATUM® (NOAA) to match the lidar data. Temperature measurements were taken every 30 min between 10 March and 18 May 2016. DTS temperatures were calibrated using a USGS stream gauge as a temperature reference. Double-ended calibration (van de Giesen et al., 2012) yielded a maximum duplexing root mean square error (RMSE) and mean bias (Hausner et al., 2011) of 0.34 °C and $9.4 \times 10^{-6}$ °C, respectively. In an unbiased sample, the RMSE is equivalent to the standard deviation, indicating that the true temperature of the cable is 95% likely to be within 0.68 °C (2 standard deviations) of the DTS-observed temperature.

Calibrated DTS temperatures were used to assess the presence or absence of snow at each point along the cable. Snow was assumed to be present if (a) the daily mean absolute value of temperature was less than or equal to 1 °C and the daily standard deviation of observed temperatures was $< 0.353$ °C. This daily standard deviation threshold corresponds to a diurnal temperature range of 1 °C, if a sinusoidal diurnal signal is assumed, similar to methods employed by Raleigh et al. (2013). DTS data were mapped at a spatial sampling rate of 0.25 m, providing the ability to resolve temperature changes over 0.50–0.75 m (Tyler et al., 2009) – finer than the 1 m pixel resolution of the lidar data. More details on the DTS measurements and data processing are given in the Supplement.

### 2.4. fSCA and k factor calculation

We applied the 1-m snow presence and absence observations derived from lidar and DTS in order to develop estimates of fSCA and a newly developed fSCA under-canopy correction factor, $k$ (Eq. (3) below). fSCA could be independently estimated as the fraction of snow covered versus snow free 1-m pixels classified as open versus canopy-covered without low vegetation. The fSCA estimates and canopy corrections were primarily analyzed and shown over 10-m grids to better accentuate the effects of topography, but were computed at 100 m and 1000 m grids to study scaling effects. The fSCA under-canopy correction factor, $k$, was defined as the ratio of fSCA under the canopy to fSCA in the open:

$$k = \frac{fSCA\_canopy}{fSCA\_open} \tag{2}$$

Most operational fSCA products assume that $k = 1$. We then developed two-dimensional linear interpolation based on the $k$ factors within each southwestness/elevation bin, separately for each ASO flight, i.e. the $k$ factors are also dependent on the date. The $k$ factors for each ASO flight were then mapped to the terrain at 10 m resolution as a function of southwestness and elevation. Next, *fSCA_open* was determined for each 10 m pixel from the 1 m ASO-based binary snow determinations. *fSCA_corrected* for each 10 m pixel was then calculated as:

$$fSCA\_corrected = (fSCA\_open^{*}k) * fVEG + fSCA\_open^{*}(1 - fVEG) \tag{3}$$

Eq. (3) is therefore applied on a per-pixel basis at 10 m spatial resolution. We compare the *fSCA_corrected* estimates from spatially variable $k$ factors against the typical assumption that $k = 1$ to illustrate bias.

We assessed the sources of uncertainty in our new lidar-derived fSCA estimation method in several ways. Lidar vertical uncertainty sources are presented in the Supplement Sect. 1 and discussed in Sect. 4. One of the primary sources of uncertainty is the number of both snow-on and snow-off returns that penetrate the forest canopy and return information about the snow surface and low vegetation, respectively. We counted the number of valid returns in the open and under the canopy for each southwestness bin and discuss the implications on uncertainty (Supplement Fig. S1 & S2; Sect. 4). Because we developed relationships for the southwestness-elevation bins, rather for each individual 10-m pixel, we were able to distribute the $k$ factor to 10 m pixels with known topography but limited under canopy returns. In order to assess the uncertainty of the fSCA corrections factors, $k$ (Eq. (3)), and test whether they were statistically significantly different from $k = 1$, bootstrapping was employed by repeatedly removing non-overlapping 10% of the valid observations in each southwestness/elevation bin, and performing the $k$ calculation with the remaining 90% of the data. The non-parametric sign test was performed on the thus obtained sample of ten $k$ factors in each bin, testing whether the median $k$ was significantly different from unity. Finally, recognizing that not all 1-m pixels are available within each coarser resolution pixel to compute fSCA and $k$, we employed a Monte Carlo theoretical simulation to estimate the associated uncertainty in the estimation of fSCA in the open and under the canopy and the $k$ factor for different availability of pixel-

level 1-m data (i.e. lidar returns under canopy), as well as spatial resolutions of 10 and 100 m.

## 3. Results

### 3.1. Site climate and snowpack in 2016

The 2015–2016 December–February temperature at the 1962 m SNOTEL (station #540) was −0.60 °C, at the 2128 m SNOTEL (station #539) was −0.57 °C, and at the 2541 m (station #541) it was −1.37 °C. Station locations are shown in Fig. 1A. All SNOTEL stations showed periods above freezing through the winter months (Fig. 1D). Upon inspection, snowpack characteristics exhibited differential melt in open vs. canopy locations (Fig. 1B), illustrating the need for quantifying these differences at the watershed scale. Snow water equivalent (SWE) at three different elevations in the Sagehen vicinity varied strongly by station elevation (Fig. 1C). Specifically, the maximum SWE at ~2500 m was ~5–6 times larger than the maximum SWE near 2000 m elevation. In addition, the maximum SWE occurred 30–50 days later in the season, and snow disappearance occurred 50–70 days later at the highest elevation compared to the lower elevations. The sampling by the three ASO lidar overflights (black dashed vertical lines in Fig. 1C & D) occurred during the ablation season at the lower elevations, and captured near-peak accumulation and the beginning of ablation at the higher elevations. The progression of snow ablation is evident in the lidar derived snow depths for March 26, April 17 and May 18, 2016 (Fig. 3A–C). The lidar-derived snow depths showed snow free areas even on March 26, 2016 (Fig. 3A) in contrast to the more sheltered SNOTEL stations that sit in large forest gaps (Fig. 1C). By May 18, only the higher elevations exhibited widespread snow coverage, while snow at lower elevations was preserved longer on the north-facing, southern edge of a meadow and in small forest gaps (Fig. 3D–F).

The ASO point cloud was used to classify the 1 m pixels into four categories – snow or no snow in tall canopy without branches < 2 m and snow or no snow in open pixels (Fig. 4A–C). Areas with low canopy (i.e. branches < 2 m) were discarded from the analysis. The March 26, 2016 map (Fig. 4A) indicates that the majority of the study area is snow-covered at open and canopy pixels, while some lower elevations and high southwestness areas were snow-free. The April 17, 2016 image exhibited significant ablation in progress and substantial snow-free areas, whereas the May 18, 2016 flight had a majority of the watershed snow free. Fig. 4A–C illustrate the widespread distribution of tall canopy pixels where snow depth/presence could be detected. The majority of classified pixels were in the open for all three ASO flights, but there was a sufficiently large number of observations under the canopy (typically $> 10^4$ and with one exception $> 10^3$) to develop statistically robust comparisons against the DTS observations (Sect. 3.2; Table 1, Supplement Figs. S1 & S2).

### 3.2. DTS observations and ASO Lidar validation

The DTS mean daily temperature observations for the 1500-m cable length running to the SW direction from the instrument (Fig. 2, 0 m mark) produced reliable snow presence information for verification against the lidar-derived snow presence. The data were of high quality with almost no temperatures lower than −1 °C (Fig. 5A) and clear separation between daily variance in snow-covered and air-exposed cable temperatures (Fig. 5B). The cable segment running through Sagehen Creek was evident near the 50 m distance as a zone of near-constant temperatures > 1 °C. The daily temperature standard deviations (Fig. 5B) illustrate that there was a sharp divide between values mostly less than the threshold value of 0.353 °C and much higher values (dark red), resulting in reasonable snow presence classification (Fig. 5C). The temporal progression of each DTS sample point (along the x-axis) in Fig. 5C illustrated patches of snow melting and decreasing in size (appearing as rightward-pointing wedges) and eventually disappearing. Some snow-free regions were present very early in the season and may be a consequence of logs and debris that the DTS cable crossed. Both open and under canopy fSCA was determined from DTS observations as the fraction of open or tall canopy pixels overlaying the DTS cable that were snow-covered (Fig. 5D). DTS-determined fSCA was near one in mid-March but fSCA under canopy was lower than open areas fSCA from mid-March until near snow disappearance in late April. The progressively lower fSCA values both in the open and under the canopy converge as the snow disappears. At the very end of the snow cover season in May, the under canopy fSCA values were slightly higher than fSCA in the open.

Validation of the ASO snow binary product (Fig. 4) using DTS snow presence/absence indicated excellent correspondence between the ASO lidar and the in-situ DTS snow observations. The classification agreement both under the canopy and in open areas varied between 85% and ~96% (Table 1). There were ~3.4 DTS sample points per ASO-based 1 m pixel on average, or effectively ~1.7 independent DTS samples per ASO pixel. The DTS snow classification values falling within an ASO pixel were in agreement with each other (i.e. they all indicated either snow or no snow) in 94.2%, 95.7%, and 99.9% of the cases for the March, April and May ASO flights. The valid under-canopy returns were approximately an order of magnitude fewer than returns in open areas. However, the number of ASO lidar under canopy returns along the DTS cable (~ 100 of ~1500 total pixels) illustrated the feasibility of the lidar-based method for detecting under-canopy snow presence.

### 3.3. Watershed-scale open and under canopy fSCA and k factors

Over the entire study domain, fSCA under the canopy was smaller by 0.07 to 0.17 than fSCA in the open (Table 2). Open and under canopy fSCA were explored separately for various elevation and southwestness bins (Fig. 6A–C). Several key fSCA variability patterns were notable: fSCA values were generally higher at higher elevations, and fSCA was also higher earlier in the ablation season, which is consistent with SNOTEL observations (Fig. 1). With few exceptions, fSCA decreased with increasing southwestness. In many cases the decrease was large, e.g. from ~1 for NE-facing slopes to < 0.5 on southwest-facing slopes in the 2300–2400 m elevation range for the April ASO flight (Fig. 6B). Most southwestness/elevation bins had higher fSCA in the open than under canopy, consistent with the results for overall study-area fSCA. A notable exception occurred for the higher positive southwestness values, where fSCA under the canopy was higher than open fSCA in most elevation bins (Fig. 6A–C).

To aid in the interpretation of open and under canopy fSCA patterns, we developed a $k$ factor that is the ratio of under canopy to open fSCA (Eq. (2)). The $k$ factor was generally less than one, reflecting greater fSCA in the open than under canopy (Fig. 6D–F; Supplement Tables S3-S5, Supplement Fig. S3). $k$ was generally less than one (near 0.8) for intermediate fSCA values and for most southwestness bins and converged to unity as fSCA approaches fully snow covered earlier in the season and at higher, more sheltered locations. (Supplement Fig. S3). $k > 1$ occurred for high southwestness > 0.2, with some exceptions. Most $k$ factors were statistically different from unity at the $p < 0.05$ and $p < 0.01$ levels (Supplement Tables S3–S5). High variability of $k$ and $k$ factors > 1 occurred for lower values of fSCA in the open. fSCA values < 0.2 are often considered snow free (e.g. Hall et al., 2012; Kostadinov and Lookingbill, 2015) and the ratio $k$ is expected to exhibit higher unceratinty in such cases. Uncertainty in fSCA and $k$ estimation at various spatial aggregation scales can also result from different levels of availability (e.g. under canopy lidar returns) of 1-m binary observations within each aggregated pixel. Theoretical Monte Carlo simulations at various data availability levels indicated that the uncertainty in fSCA and $k$ indeed increased as data availability decreased (Supplement Fig. S4). However, even at low data availabilities of 20% of all pixels, the interquartile range of fSCA stayed within 0.2, resulting in reasonable interquartile ranges of $k$. The medians of both fSCA and $k$

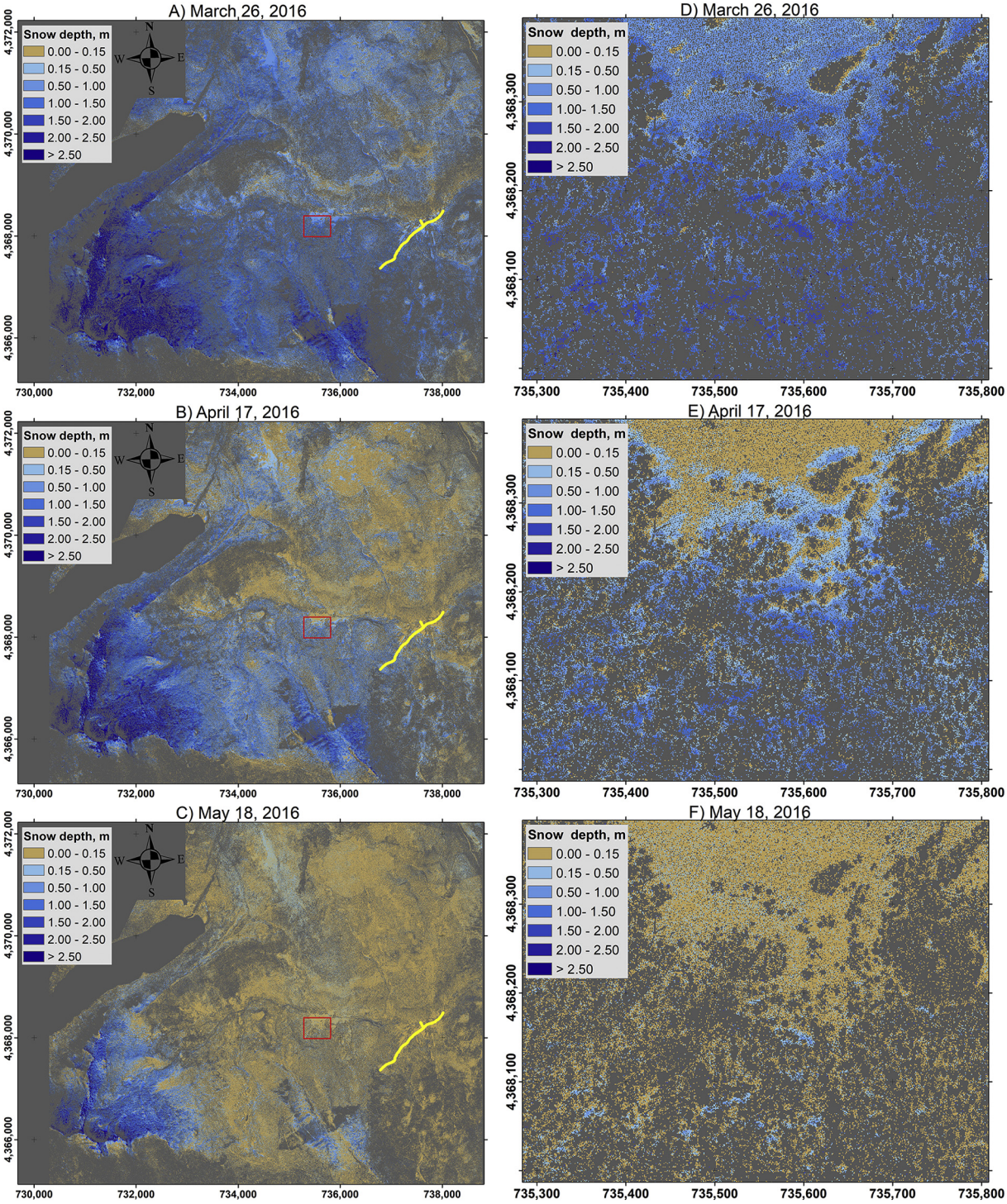


**Fig. 3.** Snow depth on a 1 m grid using ASO lidar flight data on A) March 26, 2016, B) April 17, 2016 and C) May 18, 2016. The mean elevation of all valid ASO lidar returns (those that are classified as snow or no snow, see Fig. 4) within each pixel is shown. Pixels over water and steep terrain (slope ≥ 30 °) are excluded, and all missing data and unclassified pixels are show as dark grey. A zoomed in area (indicated in a red rectangle) of the snow depth maps of A–C is shown in panels D–F, respectively. The DTS cable layout is shown in yellow in panels A–C. (For interpretation of the references to colour in this figure legend, the reader is referred to the web version of this article.)

always fell at the simulation's assigned true value. Importantly, this uncertainty in fSCA and *k* was highly scale-dependent, being much lower in the case of aggregation to 100 m resolution as compared to the 10 m case (Supplement Fig. S4).

The *k* factor's relationship with elevation and southwestness (Fig. 6D–F, Supplement Tables S3–S5 and Fig. S3) gives insight into the differential controls on snow ablation and disappearance between open and under canopy locations. The *k* factor exhibited general relationships with solar exposure that varied systematically by elevation and time of year. At higher elevations and earlier in the season (e.g. March 26), there was generally little relationship between *k* and southwestness and *k* remains near one. This reflects less solar radiation and deeper snowpacks with higher fSCA. At lower to mid elevations during the ablation season, the *k* factor was generally less than one (often about

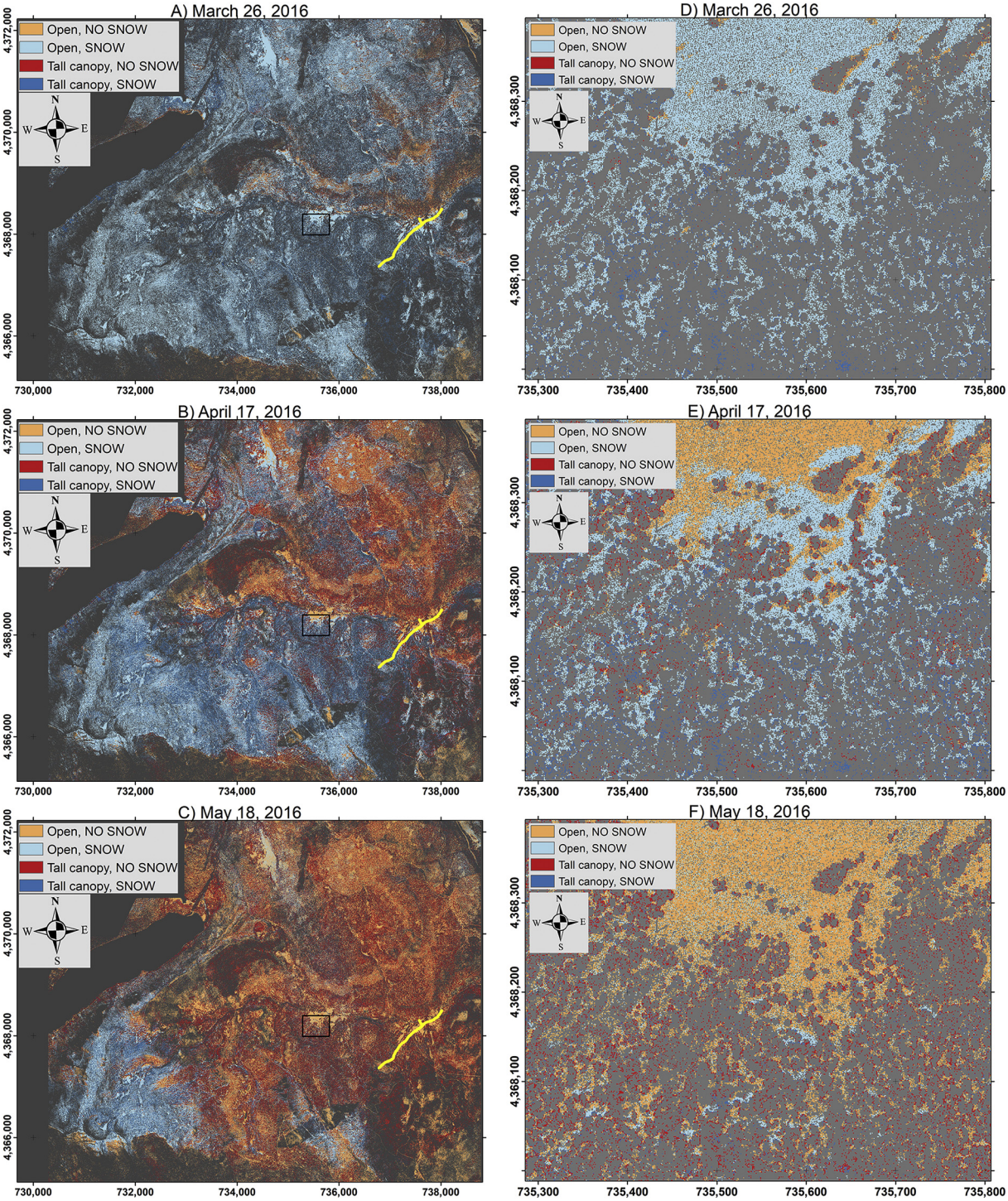


**Fig. 4.** Binary snow classification on a 1 m grid using ASO lidar flight data on A) March 26, 2016, B) April 17, 2016 and C) May 18, 2016. Pixels are classified (see legend for colour coding) according to the presence or absence of snow, and whether they represent a tall canopy or an open area according to the NCALM 2014 snow-off lidar overflight. Note that a given pixel's vegetation structure may be neither, in which case it is shown as missing data (dark grey) and is not used in the analysis. See Sect. 2.2 for details. Pixels over water and steep terrain (slope $>$ 30 °) are also excluded. The DTS cable layout is shown in yellow. A zoomed in area (indicated as a black rectangle) of the snow presence/absence maps of A–C is shown in panels D–F, respectively. (For interpretation of the references to colour in this figure legend, the reader is referred to the web version of this article.)

0.8) for southwestness values $<$ 0.2, reflecting greater snowpack ablation under canopy than in the open driven by incoming solar radiation. $k$ factors $>$ 1.0 tended to occur for high southwestness values $>$ 0.2 and at lower elevations and later in the ablation season, indicating that the final remaining patches of snow tended to occur under the canopy (where they are sheltered from stronger shortwave exposure in southwest-facing terrain and later in the season), after snow had nearly completely melted on the more exposed aspects. These observations of differential under canopy and open fSCA driven by their energy environment have implications for assumptions about the role of radiation and interception in determining snow disappearance (Lundquist et al., 2013). These systematic differences also hint at the opportunity to

**Table 1**
Validation of lidar snow cover determinations with in-situ distributed temperature sensing (DTS) measurements. The percentage of pixels over which the DTS and lidar agree as to the binary snow cover classification (snow or no snow) under canopy, in the open and overall are shown separately for each ASO flight date – March 26, April 17 and May 18, 2016. The number of agreeing pixels and the total number of pixels with valid DTS and ASO coincident observations are shown in parentheses after the percentage. For perspective, there were a total of 2344 total lidar-based 1-m pixels containing any DTS data point.

| | March % | April % | May % |
|---|---|---|---|
| Agreement canopy | 89.7% (61/68) | 85.0% (142/167) | 92.8% (129/139) |
| Agreement open | 93.2% (690/740) | 86.3% (648/751) | 97.0% (736/759) |
| Overall agreement | 92.9% (751/808) | 86.1% (790/918) | 96.3% (865/898) |

develop a canopy-correction scheme that can be applied to remote sensing snow products. In addition, we note that there was no clear relationship between fVEG and the $k$ factors (not shown).

We applied the $k$ factor to the ASO lidar-derived fSCA maps to estimate biases in under canopy fSCA and explore the potential to correct larger scale biases in satellite-derived fSCA estimates. Across the overall study area (Fig. 1A), fSCA was corrected from 0.919 (when $k = 1$ is assumed) to 0.890 (when our variable $k$ factor is applied, Eq. (3)) in March, from 0.643 to 0.590 in April, and from 0.286 to 0.272 in May, respectively. The correction always decreased the fSCA, reflecting the lower fSCA and earlier snow disappearance under the forest canopy in the majority of the study area (Fig. 7). These differences were all statistically significant according to the two-sample paired $t$-test and the

**Table 2**
Fractional snow-covered area (fSCA) as determined for the whole study domain (Fig. 1A) for the three 2016 ASO lidar overflights.

| | March 26, 2016 | April 17, 2016 | May 18, 2016 |
|---|---|---|---|
| Open | 0.92 | 0.64 | 0.29 |
| Under canopy | 0.83 | 0.47 | 0.22 |
| Difference (open - canopy) | +0.09 | +0.17 | +0.07 |

Wilcoxon rank-sum test at the 95% significance level ($p \sim 0$). The absolute difference between corrected and uncorrected fSCA was largest (~0.05) in April. The magnitude of the fSCA correction increased as $k$ diverged from one, vegetation fraction increased, and fSCA was higher. The differences between *fSCA_corrected* and *fSCA_open* are mapped in Fig. 7D–F and were consistent with the maps of $k$ factors (Supplement Fig. S5), e.g. both March and April exhibit fSCA decreases after correcting with the $k$ factor. On the other hand, May exhibited both decreases and increases in fSCA after correction. Notably, southwest-facing areas at all elevations and all areas in the lower elevation band of 2000–2100 m exhibited fSCA increases due to the correction. While the corrections to watershed-scale fSCA were generally < 0.1 absolute fSCA, corrections to individual pixels could exceed 0.3 at the 10-m resolution scale (Fig. 8), and indicated the potential value of this correction method when working at finer spatial scales.

## 4. Discussion

Snow disappearance timing and fSCA are fundamental to

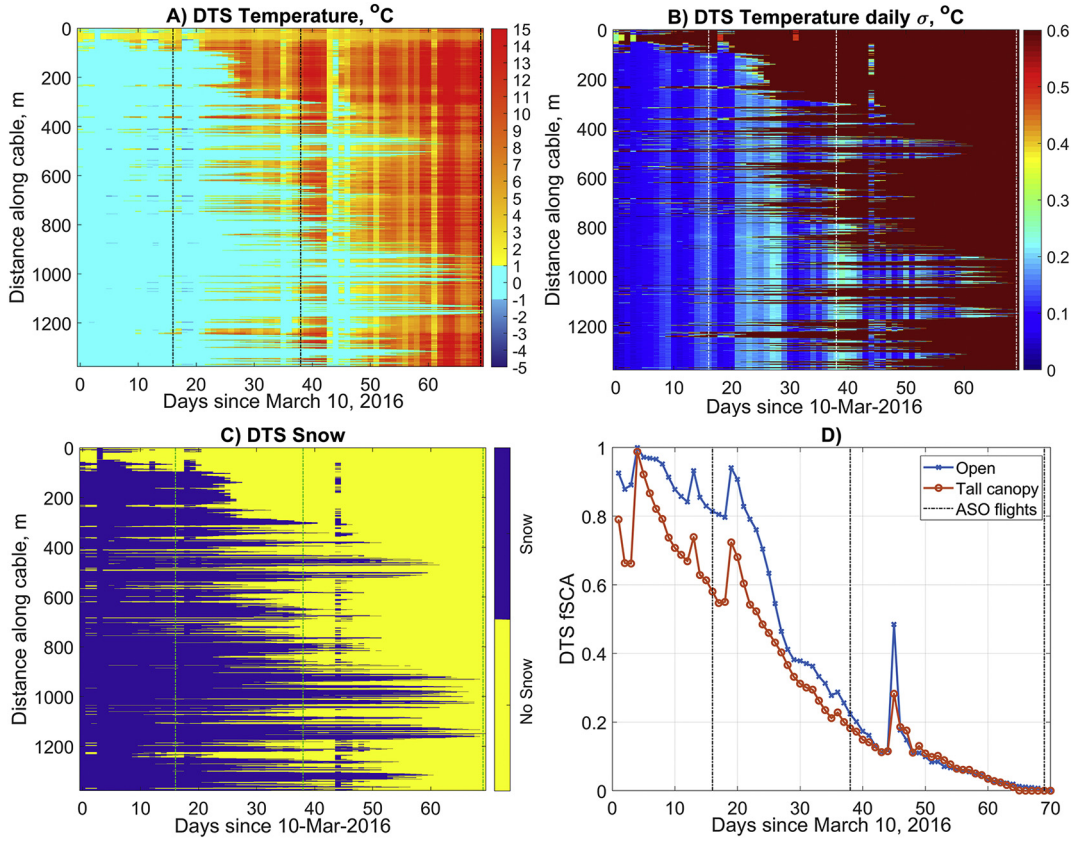


**Fig. 5.** A) DTS temperature as a function of time (x-axis) and distance along the cable (y-axis, starting at 0 m at the DTS instrument assembly, only the longer cable running SW of the instrument is shown) – the daily mean of temperature is plotted. B) Daily standard deviation of the DTS temperatures as a function of time and distance along the cable. C) The DTS snow presence classification on a daily time scale, as a function of time and distance along the cable. D) Time-evolution of fSCA over the DTS cable, as determined by DTS points falling under tall canopy vs. open areas (at 1 m pixel resolution). The three dash-dot vertical lines in all panels indicate the timing of the ASO lidar overflights (black in panels A and D, white in panel B, and green in panel C). (For interpretation of the references to colour in this figure legend, the reader is referred to the web version of this article.)

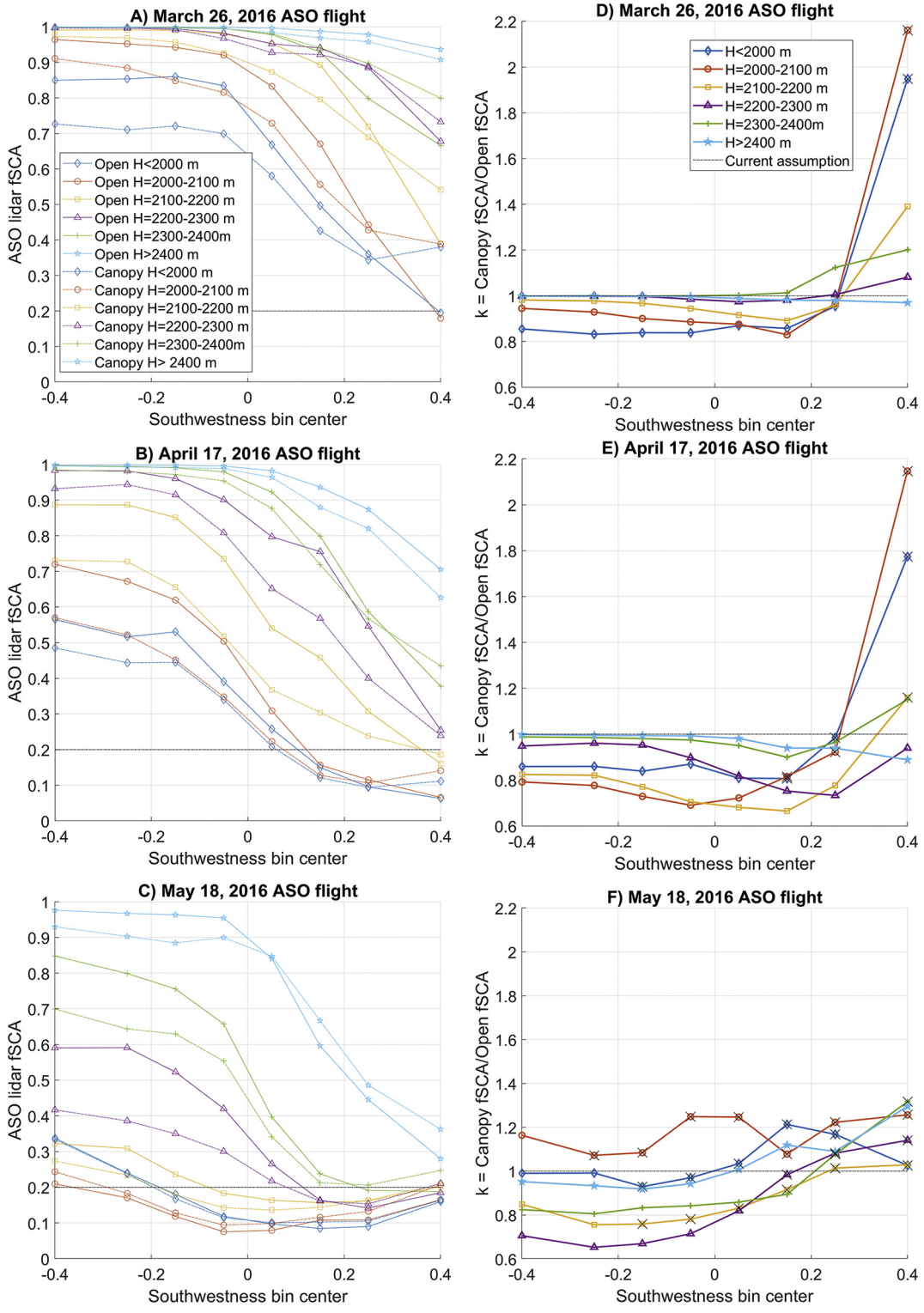


**Fig. 6.** ASO lidar-determined fSCA as a function of vegetation cover (canopy vs. open areas), southwestness, and elevation band for the A) March 26, B) April 17 and C) May 18, 2016 ASO flights. The legend in A) applies to panels B and C as well. The fSCA = 0.2 threshold is plotted as a black dash-dot line. The corresponding ratio of fSCA under the canopy to the fSCA in the open areas, i.e. the fSCA canopy correction factor *k*, is plotted in panels D-F for March, April and May, respectively, as a function of southwestness and elevation bin. The legend in panel D applies to panels E and F as well. The current operational assumption of $k = 1$ is plotted as a dash-dot black line for reference. Black 'x' drawn over the symbols in panels D-F signify that the underlying open or canopy fSCA was $< 0.2$, indicating higher uncertainty in the *k* factor. (For interpretation of the references to color in this figure legend, the reader is referred to the web version of this article.)

understanding ecohydrological processes (e.g. Lundquist et al., 2013, Harpold et al., 2014, Harpold et al., 2015b) and underlie the development and verification of numerous snowmelt modeling techniques (e.g. Molotch and Margulis, 2008; Carroll et al., 2001; Slater et al., 2013; Wrzesien et al., 2017), but are challenging to directly observe under forest canopy. Our newly developed lidar-based technique for mapping fSCA under canopy and in the open has two clear applications. First, the larger spatial footprint means that under canopy snow processes can be

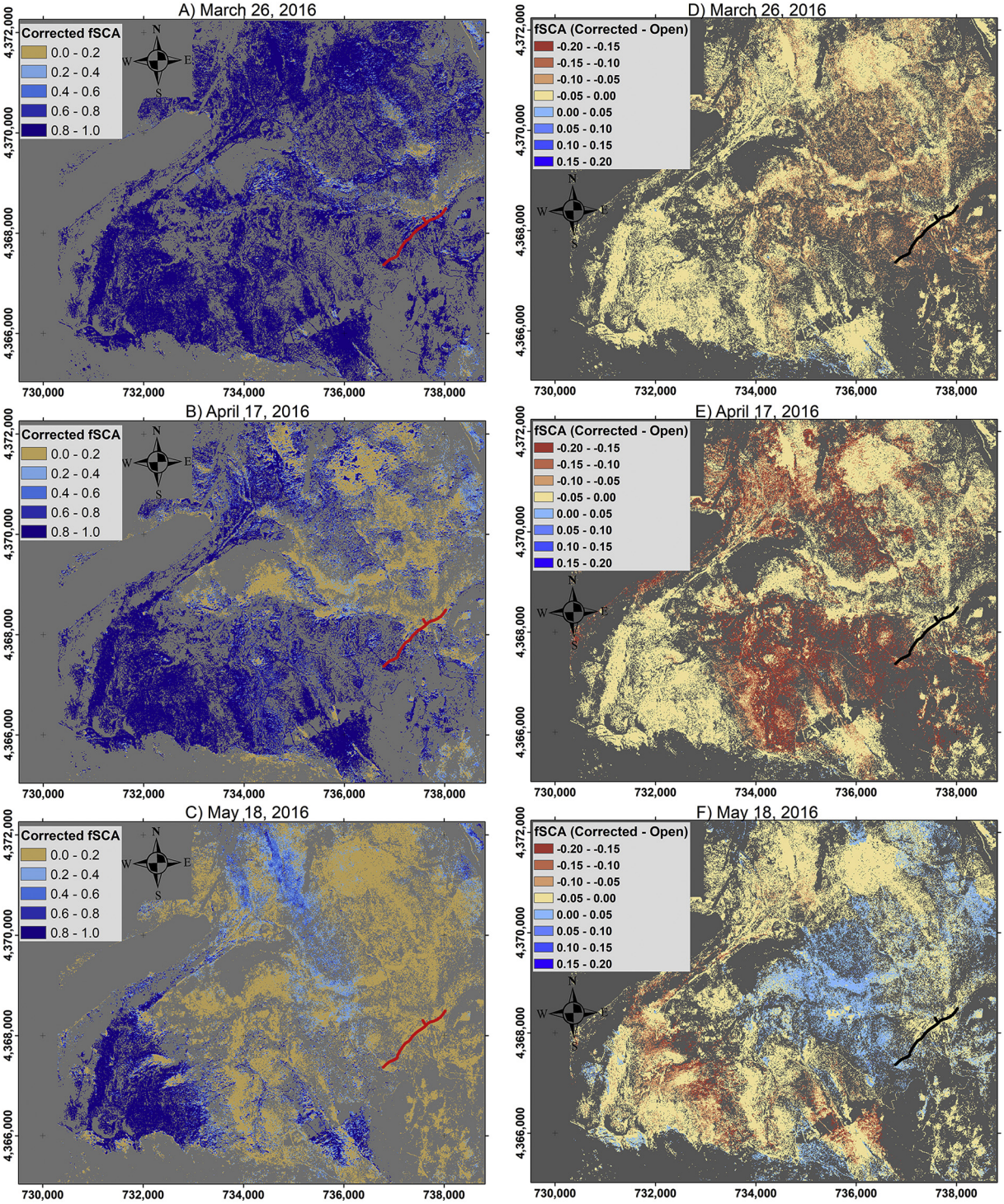


**Fig. 7.** The corrected overall fSCA at the 10 m scale for the A) March 26, 2016, B) April 17, 2016, and C) May 18, 2016 ASO lidar flights. The correction uses Eq. (3). The fVEG map used in the correction is shown in Fig. 2C, and the correction factors used are shown in Supplement Fig. S5. Maps of the underlying fSCA in the open used in Eq. (3) look visually similar at this scale and are not shown. The differences between the corrected fSCA and the fSCA in the open are shown in panels D-F for the March, April and May ASO flights, respectively (open subtracted from corrected fSCA). The DTS cable layout is shown in red in panels A–C and black in panels D–F. (For interpretation of the references to colour in this figure legend, the reader is referred to the web version of this article.)

investigated across topographic and vegetation structure gradients that were not previously possible with in-situ observations. Second, relationships between snow disappearance under canopy and in the open, summarized as our *k* factor, could be used to correct fSCA estimates that are routinely made with passive optical retrievals on a coarser spatial scale, e.g. from MODIS-type sensors. However, analysis of scale dependence (Fig. 8) indicated that the correction factor is scale-dependent and more variable and important at smaller spatial scales (higher resolutions), but also more sensitive to a lack of under canopy lidar returns. This implies that potential correction schemes based on the *k*-factor analysis presented here will be more important for future optical missions and for targeted regional surveys of higher spatial resolution. Given the potential of our lidar-based technique, we discuss the validation of the method and its limitations, as well as remaining hurdles to

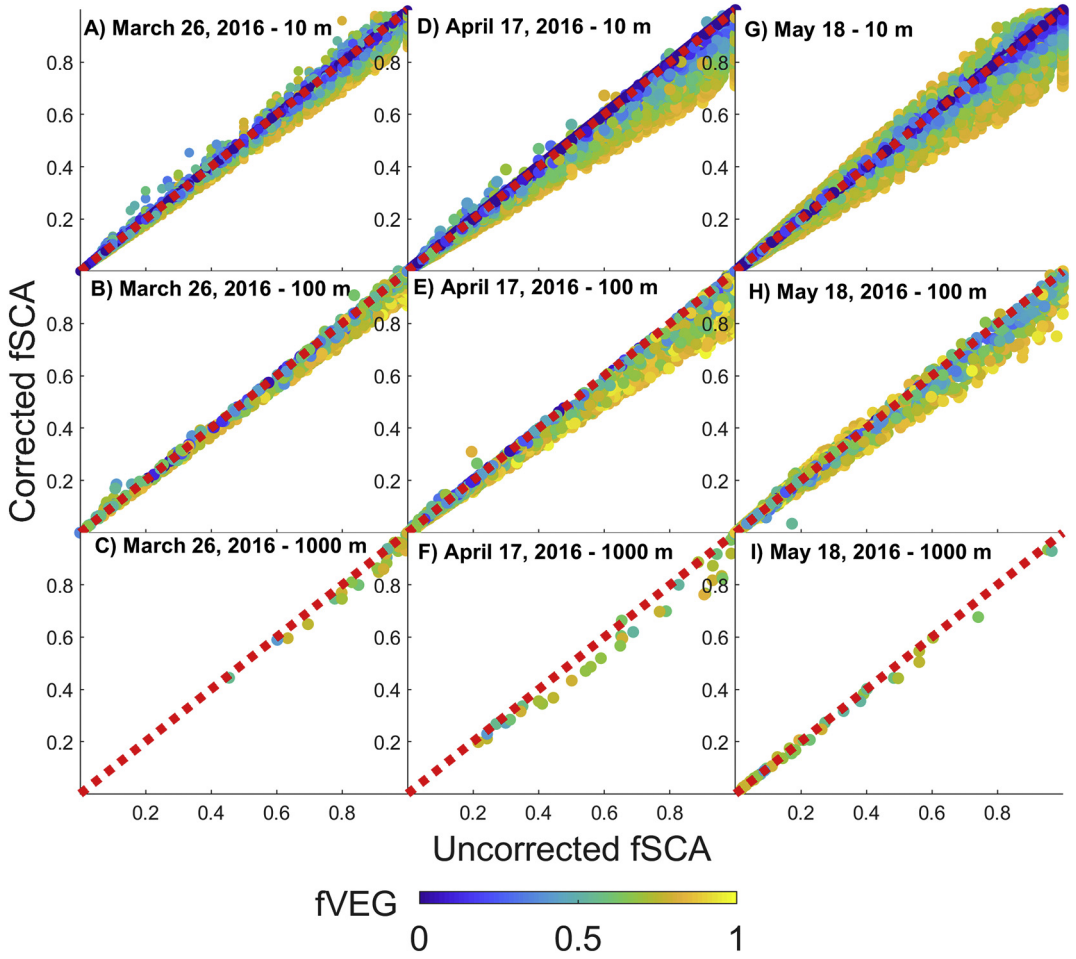


**Fig. 8.** Comparison between corrected fSCA (using the *k* factor, Eq. (2)) and uncorrected (i.e. open) fSCA at different spatial scales – 10 m (top row, panels A,D, G), 100 m (middle row, panels B,E, H), and 1000 m (bottom row, panels C,F,I), for the ASO lidar data from March 26, 2016 (panels A–C), April 17, 2016 (panels D-F), and May 18, 2016 (panels G–I). The red dotted line is the 1:1 line, and the colour mapping of each data point represents the value of fVEG coarsened to the respective scale (colorbar given at the bottom). Each point corresponds to a pixel in the respective image. Original 10 m data were aggregated to the coarser spatial scales using the mean of the underlying pixels. (For interpretation of the references to colour in this figure legend, the reader is referred to the web version of this article.)

more fully utilize our technique in these two application venues.

We used in-situ DTS measurements of snow presence to verify the prevalence and accuracy of under canopy lidar returns. ASO lidar data has not yet been validated with in-situ measurement in steep and forested terrain (field validation survey analysis is in progress (Painter et al., 2016)). Thus our validation with DTS measurements presented here is, to our knowledge, the first published ASO lidar data field validation under the canopy. While we found challenges in operating and georeferencing the DTS system (Dickerson-Lange et al., 2015), it is difficult to imagine a more suitable validation dataset for lidar because the observations are < 1 m resolution and can cover large extents. The DTS observations allowed verification of accuracy of snow presence and absence both in the open and under the canopy, as the DTS is laid out through the conifer forest (Fig. 2). The agreement between our lidar-derived snow presence and that from the DTS observations was excellent. There was similar agreement (> 85%) in both open and under canopy location, supporting the robustness of the lidar observations. Another concern with our method is that all 1-m lidar pixels with vegetation returns < 2 m were discarded, reducing the density of under canopy information. Despite fewer valid observations under canopies, we had a sufficiently large number of pixels with valid observations in every southwestness/elevation bin (Supplement Figs. S1 and S2). However, fSCA accuracy could be degraded when there are not sufficient returns and/or the spatial resolution is very fine. Given the robust validation results found here using the relatively sparse ASO lidar returns (< 2 points per $m^2$), we believe this lidar-based method will be widely transferrable to other areas with taller trees and/or denser canopies.

Two main limitations challenge the transferability of our lidar-based method to other areas: 1. Horizontal and vertical lidar registration and accuracy issues and other uncertainty sources, and 2. Choices in the open and under canopy classification systems. Lidar snow depth estimates have error that propagates from both snow off and snow on elevation estimates (Deems et al., 2013). Accurately co-registered snow depth products typically have root-mean-square error (RMSE) of around 10 cm, but often require post-processing (Harpold et al., 2015a). For example, our ASO datasets had to be spatially offset ~20–35 cm in order for the snow on and snow off road surface to match. This type of spatial bias is common and can arise from a variety of factors. The need for such adjustments due to co-registration issues represents a limitation of lidar-based snow determinations. The availability of a single reliable area of the image (Hwy 89 in the NE corner of the study domain) to determine the offsets for the entire study area could also be an additional source of uncertainty. These sources of uncertainty in lidar elevation are discussed and quantitative estimates are provided in the Supplement Sect. 1. Summer vegetation can also complicate ground detection during snow-off lidar flights (Bühler et al., 2016). The second set of limitations in our method arise from how we classify snow presence and define potential under canopy and open locations. We applied a 15 cm threshold of snow depth to define snow presence, i.e.

depths of < 15 cm are considered snow free. This threshold is loosely based on previous measurements of lidar-derived snow depth accuracy (Deems et al., 2013; Harpold et al., 2015a) and on our own best estimates of the elevation uncertainty from various sources (Supplement Sect. 1). The uncertainty in bare earth and snow on elevation increases dramatically above 30 degrees slope (Takahashi et al., 2005; Tinkham et al., 2012), which necessitated excluding steep pixels from the lidar analysis. In addition, values of fSCA below ~0.2 are generally considered unreliable (Hall et al., 2012) and would also bias the *k* factor because the denominator of Eq. (2) approaches zero. Another major limitation is differentiating low branches from the snow surface in under canopy locations. To address this challenge, we applied a 2 m vegetation height threshold over which we exclude pixels from our snow cover analysis. We found that the large number of ASO returns under canopy (Supplement Figs. S1 & S2) ensured that discarding pixels with low branches would still allow for fSCA estimation under the canopy. Sufficient ASO and NCALM lidar point density to allow vegetation and binary snow classification at 1 m scale ensures that fSCA can be estimated at the 10 m scale and since the *k* factor was computed via interpolation from terrain variables only, the fSCA correction can be applied for any 10 m pixel where *fSCA_open* and *fVEG* can be estimated. Future applications of our method will need to consider these assumptions. For example, the threshold may need to be changed for areas where snow depth or bottom height of branches is routinely well below or above 2 m. Despite the subjective nature of some these assumptions that were tuned to the Sagehen field site, the method appears robust and transferrable to other locations.

The lidar point sampling used in this analysis was spatially aggregated to 1 m resolution to create the underlying binary snow presence/absence data (Fig. 4), whereas the fSCA analysis and *k* factor computation was done primarily at 10 m and also at 100 m and 1000 m resolution. It is important to assess the effects of spatial scale on our results and hence, the applicability to sensors with similar spatial resolution, like Sentinel 2, and those with coarser resolution such as MODIS. Comparisons between uncorrected and corrected fSCA at different spatial scales, namely native 10 m, and coarsened to 100 m and 1000 m (Fig. 8), indicated that the largest differences were found at the 10 m scale for higher fSCA values later in the ablation season, and differences larger than fSCA of 0.2 were still found at 100 m scales. At 1000 m scales the *k* factor correction was smaller and likely not of large hydrological importance (but still leads to statistically significant fSCA differences at the scale of the entire study domain – see Sect. 3.3). This demonstrates that future analyses need to explicitly take spatial scale into account and design the correction accordingly for the target sensor. It is evident from Fig. 8 that the *k* factor correction is likely to be most important for high spatial resolution sensors, underscoring its importance for future satellite missions that will collect optical and spectral information at sub-100 m scales.

A source of uncertainty in fSCA and thus, in estimating the *k* factor, is the sparsity of valid binary 1-m pixels within each spatially aggregated fSCA pixel. This sparsity stems from multiple factors – thick canopies decrease the number of lidar returns penetrating to the ground or snow below, steeper slopes are excluded from the analysis, as are pixels with low branches identified by the snow-off flight (< 2 m) but the tradeoffs in these choices are hard to evaluate. Monte Carlo simulation of the effects of varying data availability on fSCA and *k* estimation at 10 and 100 m scales (Supplement Fig. S4) indicated that decreasing data availability resulted in no detected bias in the median, but increasing interquartile ranges, as expected. The actual data availability for the 10 m analysis reported here is mapped in Supplement Fig. S6, indicating that individual 10 m pixels often exhibited low data availability, and for a significant fraction of the image availability was about 30–40%. This is partially due to the relatively low point density of ASO lidar surveys (< 2 points/$m^2$). At 40% data availability fSCA can be estimated within ~ 0.15 at 10 m scales, and within < 0.02 at 100 m scales, resulting in reasonable *k* estimates with few outliers. These Monte Carlo results suggest that future lidar missions need to be conducted at higher point density (e.g. Harpold et al., 2014), in order to increase the likelihood of canopy penetration and decrease this kind of uncertainty. An additional consideration regarding data sparsity is the computation of fSCA in the open for pixels where fVEG > 90% (~30% of our 10 m pixels), including those for which fVEG = 100% (~7% of the pixels) (Fig. 2C). In these cases, we did not compute fSCA open and thus Eq. (3) cannot be applied. This is because we required at least 10 valid 1-m pixels in order to compute a value at the 10 m scale. Future operational approaches will need to consider methods to include such pixels in the analysis, e.g. by relaxing the 90% threshold and/or using neighboring pixels for fSCA in the open estimates.

Passive optical-based satellite fSCA estimates typically make assumptions about under canopy snow cover (that is hidden from their view) that can reduce their accuracy (e.g. Molotch and Margulis, 2008; Painter et al., 2009; Rittger et al., 2013). Some approaches consider forest transmissivity explicitly in the treatment of reflectance (Metsämäki et al., 2012). Romanov et al. (2003) present a model that retrieves fSCA using spectral mixture analysis and explicitly differentiate the fSCA visible to a satellite sensor from the true fSCA in a forest that is more useful for hydrological applications. However using a typical assumption that fSCA in the open and under canopy are equal ($k = 1$), we found differences between open and under canopy fSCA were in excess of ~0.15 in some southwestness/elevation bins (Fig. 6A–C) and as high as 0.35 for individual pixels at the 10 and 100 m spatial scale (Fig. 8). There was no relationship between under canopy fSCA and fVEG (not shown), but as expected the effects of the *k* factor were greatest in high fVEG areas where the under canopy returns had more influence. These results suggest that biases in under canopy fSCA assumptions are likely to increase using finer scale fSCA products that are currently under development, e.g. from sensors with higher spatial resolution. As the fSCA information and its application become more sophisticated (e.g. Slater et al., 2013; Kahl, 2013; Bair et al., 2016), better treatment of under-canopy processes will be key to maximizing the information extracted from satellite imagery.

The consistent differences between *k* factors from different elevation and southwestness bins reflect underlying differences in snowpack energetics caused by the forest canopy and its interaction with the atmosphere mediated by local and remote terrain. Forests strongly modify the snowpack energy balance through counteracting influences – decreasing shortwave radiation by shading, which helps to retain snowpack, and increasing longwave radiation by emissions from tree trunks and canopies, which acts to warm and ablate the snowpack (Lundquist et al., 2013). The relative dominance of shortwave versus longwave is sensitive to forest canopy structure (e.g. Broxton et al., 2014; Seyednasrollah and Kumar, 2014; Webster et al., 2017), as well as latitude, elevation, slope and aspect, cloudiness and humidity, and day of year (i.e. solar declination). Note that in addition to longwave vs. shortwave balance, canopy interception also plays a role in reducing snow depth and accelerating snow disappearance under the canopy (Hedstrom and Pomeroy, 1998; Storck et al., 2002; Moeser et al., 2016; Dickerson-Lange et al., 2017). Lundquist et al. (2013) developed a data-based conceptual model to argue that sites with December–February (DJF) temperatures above −1 °C were likely to retain snow longer in the open than under canopy. This pattern of longer snow retention in the open in warmer sites is driven by warmer air temperatures leading to correspondingly warmer canopy temperatures and thus, greater longwave radiation from the canopy. The three SNOTEL stations used in this study spanned this key threshold during 2015–2016, with the 1962 m and 2128 m SNOTELs just warmer than the −1 °C threshold and the 2541 m SNOTEL was just colder than the −1 °C threshold. Our widespread finding of earlier snow disappearance in under canopy positions (i.e. *k* factors statistically < 1), is consistent with the Lundquist et al. (2013) model for sites warmer than −1 °C. However, our spatially explicit *k* factors show that areas in the highest elevation bin, with DJF temperatures < −1 °C, only preserved snow longer in

under canopy where southwestness > 0 (cyan curve for > 2400 m elevation with stars in Fig. 6F). The May $k$ factors > 1 in high solar exposure areas > 2400 m in elevation are inconsistent with the Lundquist et al. (2013), model because these sites should be warmer than −1 °C and therefore have $k$ factors < 1. These inconsistencies suggest that a simple temperature-based threshold for predicting differential snow disappearance under canopy may not be sufficient for explaining details of intra- and inter-site differences (e.g. variations in radiation that are driven by local and remote terrain shading, latitude, and cloudiness). Similarly, we found that snow was retained longer in under-canopy areas in high-energy environments during low fSCA conditions in many of the lower elevation bins. We attribute this to a shift from the trees acting to ablate the snow through longwave radiation to the trees creating shaded zones where ablation is lower during higher sun altitudes in May. Generally, elevation appeared to be a secondary factor to southwestness in determining $k$ factor variability at our site. While as expected elevation determined the timing and amount of accumulation and ablation, $k$ varied more strongly in space with the absolute value of fSCA and southwestness (Fig. 6, Fig. S3). This emphasizes that a simpler temperature (i.e. latitude/elevation) based model, such as the Lundquist et al. (2013), would miss the spatial variability in $k$ with local topography. Finally, $k$ factors > 1 occurred most frequently where fSCA values < 0.2 (Supplement Fig. S3) causing high uncertainty but minimal hydrological effects. These findings illustrate the potential new inferences into snow-forest interactions from our new high spatial resolution technique within a single watershed.

One potential application of our lidar-based method is to operationalize the $k$ factor (Eq. (3)) to achieve better estimates of landscape fSCA in montane forests. Development of our $k$ factor method would not be possible using ground-based observations, which typically only have < 5 paired observations in open and under canopy areas (e.g. Lundquist et al., 2013; Dickerson-Lange et al., 2017). Most landscapes would be expected to have consistent patterns in $k$ factors year-to-year dictated by climate, topography, and existing forest structure. However, $k$ factors are not expected to be constant in time, as is demonstrated here by the three lidar overflights capturing the ablation season (Fig. 6A–C). Furthermore, the temporal evolution of $k$ factors is expected to shift year to year even for the same site, due to interannual variability in the size and cold content of the snowpack, as well as the cloudiness, wind, humidity, and temperature during the ablation season. Both between-site and within-site spatial and temporal variability would need to be addressed before this approach can be robustly operationalized over continental scales. The formulation of Eqs. (2) and (3) implies that if $fSCA\_open = 0$, then $fSCA\_canopy = 0$ for any $k$. Operational application to areas for which snow ablates primarily in the open faster than under the canopy (e.g. cold forests) will need to consider ways to address this for the limiting case when snow in the open has fully disappeared. More applications of our method across different climate zones (and ideally multiple years) could be used to develop relationships between the $k$ factor and physiographic and topographic variables, akin to the approach of Lundquist et al. (2013) but including topography and forest canopy properties. Several additional major challenges exist to operationalize the $k$ factor that may make it suitable for certain applications. For example, the $k$ factor may be sensitive to sensor view angle and its interaction with topography, e.g. for MODIS (Dozier et al., 2008). Overall, these types of corrections will prove most important for sensors with higher spatial resolution (Fig. 8) and less view angle issues, like Landsat, Sentinel-2, and future similar missions. An operational $k$ factor map based on relationships to topography and climate, combined with a decadal snow-off lidar survey to establish vegetation structure and the DEM, could be an important tool to improve daily or weekly operational satellite products in dense, montane forests with relatively little investment.

## 5. Conclusions

There are few tools to observe snow processes under the forest canopy at fine spatial scales, which limits process understanding and application of satellite derived snow products. We developed a new lidar-based method to observe under-canopy fSCA and verified the method with in-situ DTS observations in the Sagehen Creek watershed in the Sierra Nevada range of California, USA. Observations of open and under canopy snow cover have generally been restricted to a handful of paired snow depth sensors or manual observations (Lundquist et al., 2013; Coons et al., 2014; Harpold et al., 2014; Dickerson-Lange et al., 2017). Our lidar-based method expanded the extent of field observations to better understand the role of topography (elevation, slope, aspect, remote shading, etc.) and time of year on differential snow disappearance between open and under canopy locations. Using a multi-temporal lidar dataset, we showed that the expected earlier snow disappearance under canopy based on a simple model of DJF temperature (Lundquist et al., 2013) was generally correct in predicting earlier snow disappearance under forest canopy. However, the higher elevations were colder than −1 °C and melted snow earlier in under canopy position in more sheltered areas, but retained snow longer under canopy in areas with more solar exposure. Similarly, many of the last-to-melt locations were under canopy positions that benefit from canopy shading and sheltering in high-energy environments. These types of observations could help verify and improve physically-based snowmelt models. In addition, our $k$ factor (the ratio of fSCA under canopy to fSCA in the open) can be used to improve overall fSCA estimates by refining assumptions about under canopy fSCA (e.g. $k = 1$) used in optical remote sensing products. The temporal evolution of $k$ and its variability would need to be investigated further to apply our $k$ factor approach in an operational setting across sites with varying climate and topography. We demonstrated that preferential snow disappearance under canopy can make a sizable impact on fSCA at 10 and 100-m scales, particularly in areas with higher vegetation cover. We believe that future applications of our method will improve our understanding and prediction of snow-forest interactions in complex terrain and build towards better corrections of satellite-derived fSCA products in dense, montane forests.

## Acknowledgments

This work was supported by NASA grant #NNX14AN24A. Instrumentation and technical support was provided by the CTEMPs facility under NSF grant #EAR-1440596. We thank the NCALM team, the project PI Qinghua Guo and Open Topography and their NSF sponsors for collecting, processing, storing and distributing the NCALM snow-off lidar data. Part of this work was performed at the Jet Propulsion Laboratory, California Institute of Technology under contract with NASA, the funding for which came from the NASA Terrestrial Hydrology Program. We thank Jeff Brown and the Sagehen Reserve for access to field site locations. We appreciate field help by Rose Petersky, and Kasey Hewson. MATLAB®,ArcGIS®, FUSION®, and Octave® were used for data analysis and visualization. We thank Thomas Pingel for his lasread.m script, Thomas Dilts for help with GNSS data processing, and Theresa O'Halloran, Harish Vedantham, and undergraduate students in the Nevada Mountain Ecohydrology Lab for helpful discussions. The data for the background imagery in Fig. 1A is from ESRI® and their data suppliers. We thank Aslak Grinsted for his plotting scripts. Part of this work was performed at the California State University San Marcos.

## Declarations of interest

None.

## Appendix A. Supplementary material

Supplementary material to this article can be found online at https://doi.org/10.1016/j.rse.2018.11.037.

## References


Bair, E.H., Rittger, K., Davis, R.E., Painter, T.H., Dozier, J., 2016. Validating reconstruction of snow water equivalent in California's Sierra Nevada using measurements from the NASA Airborne Snow Observatory. Water Resour. Res. 52. https://doi.org/10.1002/2016WR018704.

Barnett, T.P., Adam, J.C., 2005. Potential impacts of a warming climate on water availability in snow-dominated regions. Nature 438 (7066), 303–309. https://doi.org/10.1038/nature04141.

Barnhart, T.B., Molotch, N.P., Livneh, B., Harpold, A.A., Knowles, J.F., Schneider, D., 2016. Snowmelt ratedictates streamflow. Geophys. Res. Lett. 43, 8006–8016. https://doi.org/10.1002/2016GL069690.

Berg, N., Hall, A., 2017. Anthropogenic warming impacts on California snowpack during drought. Geophys. Res. Lett. 44 (5), 2511–2518. https://doi.org/10.1002/2016GL072104.

Berghuijs, W.R., Woods, R. a, Hrachowitz, M., 2014. A precipitation shift from snow towards rain leads to a decrease in streamflow-supplement. Nat. Clim. Chang. 4 (7), 583–586. https://doi.org/10.1038/NCLIMATE2246.

Biederman, J.A., Brooks, P.D., Harpold, A.A., Gochis, D.J., Gutmann, E., Reed, D.E., Pendall, E., Ewers, B.E., 2014. Multiscale observations of snow accumulation and peak snowpack following widespread, insect-induced lodgepole pine mortality. Ecohydrology 7 (1), 150–162. https://doi.org/10.1002/eco.1342.

Biederman, J.A., Somor, A.J., Harpold, A.A., Gutmann, E.D., Breshears, D.D., Troch, P.A., Gochis, D.J., Scott, R.L., Meddens, A.J.H., Brooks, P.D., 2015. Recent tree die-off has little effect on streamflow in contrast to expected increases from historical studies. Water Resour. Res. 51 (12), 9775–9789. https://doi.org/10.1002/2015WR017401.

Böhner, J., Antonić, O., 2009. Chapter 8 Land-surface parameters specific to topo-climatology. In: Hengl, T., -D, H.I.B.T., Reuter, S.S. (Eds.), Geomorphometry. vol. 33. Elsevier, pp. 195–226. https://doi.org/10.1016/S0166-2481(08)00008-1.

Broxton, P.D., Harpold, A.A., Biederman, J.A., Troch, P.A., Molotch, N.P., Brooks, P.D., 2014. Quantifying the effects of vegetation structure on snow accumulation and ablation in mixed-conifer forests. Ecohydrology 8 (6), 1073–1094. https://doi.org/10.1002/eco.1565.

Bühler, Y., Adams, M.S., Bösch, R., Stoffel, A., 2016. Mapping snow depth in alpine terrain with unmanned aerial systems (UASs): potential and limitations. Cryosphere 10, 1075–1088. https://doi.org/10.5194/tc-10-1075-2016.

Buma, B., Livneh, B., 2015. Potential effects of forest disturbances and management on water resources in a warmer climate. For. Sci. 61 (5), 895–903. https://doi.org/10.5849/forsci.14-164.

Carroll, T., Cline, D., Fall, G., Nilsson, A., 2001. NOHRSC operations and the simulation of snow cover properties for the coterminous US. In: 69th Annual Meeting of the Western Snow Conference. 2001.

Cline, D., Rost, A., Painter, T., Bovitz, C., 2010. Algorithm Theoretical Basis Document, Snow Cover, v. 2.1. NOAA NESDIS. https://www.goes-r.gov/products/ATBDs/baseline/baseline-snow-cover-v2.0.pdf, Accessed date: 8 October 2018.

Coons, L.P., Nolin, A.W., Gleason, K.E., Mar, E.J., Rittger, K., Roth, T.R., Painter, T.H., 2014. Seeing the snow through the trees: toward a validated canopy adjustment for satellite snow-covered area. In: Remote Sensing of the Terrestrial Water Cycle, pp. 199–213. https://doi.org/10.1002/9781118872086.ch12.

Cristea, N.C., Breckheimer, I., Raleigh, M.S., HilleRisLambers, J., Lundquist, J.D., 2017. An evaluation of terrain-based downscaling of fractional snow covered area data sets based on LiDAR-derived snow data and orthoimagery. Water Resour. Res. 53. https://doi.org/10.1002/2017WR020799.

Deems, J.S., Painter, T.H., Finnegan, D.C., 2013. Lidar measurement of snow depth: a review. J. Glaciol. 59 (215), 467–479. https://doi.org/10.3189/2013JoG12J154.

Dickerson-Lange, S.E., Lutz, J.A., Martin, K.A., Raleigh, M.S., Gersonde, R., Lundquist, J.D., 2015. Evaluating observational methods to quantify snow duration under diverse forest canopies. Water Resour. Res. 51 (2), 1203–1224. https://doi.org/10.1002/2014WR015744.

Dickerson-Lange, S.E., Gersonde, R.F., Hubbart, J.A., Link, T.E., Nolin, A.W., Perry, G.H., Roth, T.R., Wayand, N.E., Lundquist, J.D., 2017. Snow disappearance timing is dominated by forest effects on snow accumulation in warm winter climates of the Pacific Northwest, United States. Hydrol. Process. 31 (10), 1846–1862. https://doi.org/10.1002/hyp.11144.

Dozier, J., Painter, T.H., 2004. Multispectral and hyperspectral remote sensing of alpine snow properties. Annu. Rev. Earth Planet. Sci. 32 (1), 465–494. https://doi.org/10.1146/annurev.earth.32.101802.120404.

Dozier, J., Painter, T.H., Rittger, K., Frew, J.E., 2008. Time-space continuity of daily maps of fractional snow cover and albedo from MODIS. Adv. Water Resour. 31 (11), 1515–1526. https://doi.org/10.1016/j.advwatres.2008.08.011.

ESA, 2018. Level-2A algorithm overview. https://earth.esa.int/web/sentinel/technical-guides/sentinel-2-msi/level-2a/algorithm (last accessed Aug. 11, 2018).

Essery, R., Pomeroy, J., Ellis, C., Link, T., 2008. Modelling longwave radiation to snow beneath forest canopies using hemispherical photography or linear regression. Hydrol. Process. 22, 2788–2800. https://doi.org/10.1002/hyp.6930.

Ferraz, A., Saatchi, S., Bormann, K., Painter, T., 2018. Fusion of NASA Airborne Snow Observatory (ASO) Lidar time series over mountain forest landscapes. Remote Sens. 10 (2), 164. https://doi.org/10.3390/rs10020164.

Garvelmann, J., Pohl, S., Weiler, M., 2013. From observation to the quantification of snow processes with a time-lapse camera network. Hydrol. Earth Syst. Sci. 17, 1415–1429. https://doi.org/10.5194/hess-17-1415-2013.

Hall, D.K., Riggs, G.A., 2007. Accuracy assessment of the MODIS snow products. Hydrol. Process. https://doi.org/10.1002/hyp.6715.

Hall, D.K., Foster, J.L., Digirolamo, N., Riggs, G.A., 2012. Snow cover, snowmelt timing and stream power in the Wind River Range, Wyoming. Geomorphology 137 (1), 87–93. https://doi.org/10.1016/j.geomorph.2010.11.011.

Harpold, A.A., Guo, Q., Molotch, N., Brooks, P.D., Bales, R., Fernandez-Diaz, J.C., Lucas, R., 2014. LiDAR-derived snowpack data sets from mixed conifer forests accross the Western United States. Water Resour. Res. 50 (October 2013), 2749–2755. https://doi.org/10.1002/2013WR013935.Received.

Harpold, A.A., Marshall, J.A., Lyon, S.W., Barnhart, T.B., Fisher, B.A., Donovan, M., ... West, N., 2015a. Laser vision: lidar as a transformative tool to advance critical zone science. Hydrol. Earth Syst. Sci. 19 (6), 2881–2897. https://doi.org/10.5194/hess-19-2881-2015.

Harpold, A.A., Molotch, N.P., Musselman, K.N., Bales, R.C., Kirchner, P.B., Litvak, M., Brooks, P.D., 2015b. Soil moisture response to snowmelt timing in mixed-conifer subalpine forests. Hydrol. Process. 29, 2782–2798. https://doi.org/10.1002/hyp.10400.

Hausner, M.B., Suárez, F., Glander, K.E., van de Giesen, N., Selker, J.S., Tyler, S.W., 2011. Calibrating single-ended fiber-optic raman spectra distributed temperature sensing data. Sensors 11 (11), 10859–10879. https://doi.org/10.3390/s111110859.

Hedstrom, N.R., Pomeroy, J.W., 1998. Measurements and modelling of snow interception in the boreal forest. Hydrol. Process. 12 (10), 1611–1625.

Hopkinson, C., Collins, T., Anderson, A., Pomeroy, J., Spooner, I., 2012. Spatial snow depth assessment using LiDAR transect samples and public GIS data layers in the Elbow River Watershed, Alberta. Can. Water Res. J. 37, 69–87.

Kahl, A., 2013. Reconstruction of Heterogeneous Snow Water Equivalent from MODIS Imagery and Energy Balance Modeling (PhD Thesis). University of California Santa Barbara.

Kostadinov, T.S., Lookingbill, T.R., 2015. Snow cover variability in a forest ecotone of the Oregon Cascades via MODIS Terra products. Remote Sens. Environ. 164, 155–169. https://doi.org/10.1016/j.rse.2015.04.002.

Li, D., Wrzesien, M.L., Durand, M., Adam, J., Lettenmaier, D.P., 2017. How much runoff originates as snow in the western United States, and how will that change in the future? Geophys. Res. Lett. 44 (12), 6163–6172. https://doi.org/10.1002/2017GL073551.

Link, T.E., Marks, D., 1999. Point simulation of seasonal snow cover dynamics beneath boreal forest canopies. J. Geophys. Res.-Atmos. 104 (D22), 27841–27857. https://doi.org/10.1029/1998JD200121.

Lundquist, J.D., Lott, F., 2008. Using inexpensive temperature sensors to monitor the duration and heterogeneity of snow-covered areas. Water Resour. Res. 46 (4), 8–13. https://doi.org/10.1029/2008WR007035.

Lundquist, J.D., Dickerson-Lange, S.E., Lutz, J.A., Cristea, N.C., 2013. Lower forest density enhances snow retention in regions with warmer winters: a global framework developed from plot-scale observations and modeling. Water Resour. Res. 49 (10), 6356–6370. https://doi.org/10.1002/wrcr.20504.

Lundquist, J.D., Chickadel, C., Cristea, N., Currier, W.R., Henn, B., Keenan, E., Dozier, J., 2018. Separating snow and forest temperatures with thermal infrared remote sensing. Remote Sens. Environ. 209, 764–779.

Lutz, J., Martin, K., Lundquist, J.D., 2012. Using fiber optic cable to measure surface temperature in heterogeneous forests. Northwest Sci. 86 (2), 108–121. https://doi.org/10.3955/046.086.0203.

Marks, D., Winstral, A., Seyfried, M., 2002. Simulation of terrain and forest shelter effects on patterns of snow deposition, snowmelt and runoff over a semi-arid mountain catchment. Hydrol. Process. 16 (18), 3605–3626. https://doi.org/10.1002/hyp.1237.

Marks, D., Winstral, A., Flerchinger, G., Reba, M., Pomeroy, J., Link, T., Elder, K., 2008. Comparing simulated and measured sensible and latent heat fluxes over snow under a pine canopy to improve an energy balance snowmelt model. J. Hydrometeorol. 9 (6), 1506–1522. https://doi.org/10.1175/2008JHM874.1.

Metsämäki, S., Mattila, O.P., Pulliainen, J., Niemi, K., Luojus, K., Bottcher, K., 2012. An optical reflectance model-based method for fractional snow cover mapping applicable to continental scale. Remote Sens. Environ. 123, 508–521. https://doi.org/10.1016/j.rse.2012.04.010.

Moeser, D., Mazzotti, G., Helbig, N., Jonas, T., 2016. Representing spatial variability of forest snow: implementation of a new interception model. Water Resour. Res. 52, 1208–1226. https://doi.org/10.1002/2015WR017961.

Molotch, N.P., Margulis, S.A., 2008. Estimating the distribution of snow water equivalent using remotely sensed snow cover data and a spatially distributed snowmelt model: a multi-resolution, multi-sensor comparison. Adv. Water Resour. 31 (11), 1503–1514. https://doi.org/10.1016/j.advwatres.2008.07.017.

Musselman, K.N., Molotch, N.P., Margulis, S.A., Kirchner, P.B., Bales, R.C., 2012. Influence of canopy structure and direct beam solar irradiance on snowmelt rates in a mixed conifer forest. Agric. For. Meteorol. 161, 46–56. https://doi.org/10.1016/j.agrformet.2012.03.011.

National Research Council, 2008. Hydrologic Effects of a Changing Forest Landscape, Barten P K (Chair). The National Academies Press, Washington DC, pp. 167.

Painter, T.H., Dozier, J., Roberts, D.A., Davis, R.E., Green, R.O., 2003. Retrieval of subpixel snow-covered area and grain size from imaging spectrometer data. Remote Sens. Environ. 85 (1), 64–77. https://doi.org/10.1016/S0034-4257(02)00187-6.

Painter, T.H., Rittger, K., McKenzie, C., Slaughter, P., Davis, R.E., Dozier, J., 2009. Retrieval of subpixel snow covered area, grain size, and albedo from MODIS. Remote Sens. Environ. 113 (4), 868–879. https://doi.org/10.1016/j.rse.2009.01.001.

Painter, T.H., Berisford, D.F., Boardman, J.W., Bormann, K.J., Deems, J.S., Gehrke, F., Hedrick, A., Joyce, M., Laidlaw, R., Marks, D., Mattmann, C., McGurk, B., Ramirez, P., Richardson, M., Skiles, S.M., Seidel, F.C., Winstral, A., 2016. The airborne snow

observatory: Fusion of scanning lidar, imaging spectrometer, and physically-based modeling for mapping snow water equivalent and snow albedo. Remote Sens. Environ. 184, 139–152. https://doi.org/10.1016/j.rse.2016.06.018.

Pomeroy, J.W., Marks, D., Link, T., Ellis, C., Hardy, J., Rowlands, A., Granger, R., 2009. The impact of coniferous forest temperature on incoming longwave radiation to melting snow. Hydrol. Process. 23 (17), 2513–2525. https://doi.org/10.1002/hyp.7325.

Pugh, E., Small, E., 2012. The impact of pine beetle infestation on snow accumulation and melt in the headwaters of the Colorado River. Ecohydrology. https://doi.org/10.2166/nh.2013.097.

Pulliainen, J.T., Grandell, J., Hallikainen, M.T., 1999. HUT snow emission model and its applicability to snow water equivalent retrieval. IEEE Trans. Geosci. Remote Sens. 37 (3), 1378–1390. https://doi.org/10.1109/36.763302.

Raleigh, M.S., Rittger, K., Moore, C.E., Henn, B., Lutz, J.A., Lundquist, J.D., 2013. Ground-based testing of MODIS fractional snow cover in subalpine meadows and forests of the Sierra Nevada. Remote Sens. Environ. 128, 44–57. https://doi.org/10.1016/j.rse.2012.09.016.

Rittger, K., Painter, T.H., Dozier, J., 2013. Assessment of methods for mapping snow cover from MODIS. Adv. Water Resour. 51, 367–380. https://doi.org/10.1016/j.advwatres.2012.03.002.

Robock, A., 1984. Snow and ice feedbacks prolong effects of nuclear winter. Nature 310, 667. https://doi.org/10.1038/310667a0.

Romanov, P., Tarpley, D., Gutman, G., Carroll, T., 2003. Mapping and monitoring of the snow cover fraction over North America. J. Geophys. Res. 108 (D16), 8619. https://doi.org/10.1029/2002JD003142.

Royer, A., Goita, K., Kohn, J., De Seve, D., 2010. Monitoring dry, wet, and no-snow conditions from microwave satellite observations. IEEE Geosci. Remote Sens. Lett. 7 (4), 670–674. https://doi.org/10.1109/LGRS.2010.2045733.

Selker, J.S., Thévenaz, L., Huwald, H., Mallet, A., Luxemburg, W., van de Giesen, N., Stejskal, M., Zeman, J., Westhoff, M., Parlange, M.B., 2006. Distributed fiber optic temperature sensing for hydrologic systems. Water Resour. Res. https://doi.org/10.1029/2006WR005326.

Serreze, M.C., Clark, M.P., Armstrong, R.L., McGinnis, D. a, Pulwarty, R.S., 1999. Characteristics of the western United States snowpack from snowpack telemetry (SNOTEL) data. Water Resour. Res. 35 (7), 2145–2160. https://doi.org/10.1029/1999WR900090.

Seyednasrollah, B., Kumar, M., 2014. Net radiation in a snow-covered discontinuous forest gap for a range of gap sizes and topographic configurations. J. Geophys. Res. Atmos. 119, 10,323–10,342. https://doi.org/10.1002/2014JD021809.

Sicart, J.E., Pomeroy, J.W., Essery, R.L., Bewley, D., 2006. Incoming longwave radiation to melting snow: observations, sensitivity and estimation in northern environments. Hydrol. Process. 20, 3697–3708. https://doi.org/10.1002/hyp.6383.

Slater, A.G., Barrett, A.P., Clark, M.P., Lundquist, J.D., Raleigh, M.S., 2013. Uncertainty in seasonal snow reconstruction: relative impacts of model forcing and image availability. Adv. Water Resour. 55, 165–177.

Small, E.E., McConnell, J.R., 2008. Comparison of soil moisture and meteorological controls on pine and spruce transpiration. Ecohydrology 1 (3), 205–214. https://doi.org/10.1002/eco.25.

Storck, P., Lettenmaier, D.P., Bolton, S.M., 2002. Measurement of snow interception and canopy effects on snow accumulation and melt in a mountainous maritime climate, Oregon, United States. Water Resour. Res. 38 (11), 1223–1239. https://doi.org/10.1029/2002WR001281.

Takahashi, T., Yamamoto, K., Senda, Y., Tsuzuku, M., 2005. Estimating individual-tree heights of sugi (*Cryptomeria japonica* D. Don) plantations in mountainous areas using small-footprint airborne lidar. J. For. Res. 10, 135–142.

Tinkham, W.T., Smith, A.M.S., Hoffman, C., Hudak, A.T., Falkowski, M.J., Swanson, M.E., Gessler, P.E., 2012. Investigating the influence of LiDAR ground surface errors on the utility of derived forest inventories. Can. J. For. Res. 42 (3), 413–422. https://doi.org/10.1139/x11-193.

Tyler, S.W., Burak, S.A., McNamara, J.P., Lamontagne, A., Selker, J.S., Dozier, J., 2008. Spatially distributed temperatures at the base of two mountain snowpacks measured with fiber-optic sensors. J. Glaciol. 54 (187), 673–679. https://doi.org/10.3189/002214308786570827.

Tyler, S.W., Selker, J.S., Hausner, M.B., Hatch, C.E., Torgersen, T., Thodal, C.E., Schladow, S.G., 2009. Environmental temperature sensing using Raman spectra DTS fiber-optic methods. Water Resour. Res. 45 (4), W00D23. https://doi.org/10.1029/2008WR007052.

USFS Region 5 Remote Sensing Lab, 2015. Full Waveform LiDAR Survey of Tahoe National Forest - Acquired Fall of 2013 and Summer of 2014. Acquired by The National Center for Airborne Laser Mapping (NCALM), PI: Qinghua Guo, Ph.D., in Agreement with USFS Region 5 Remote Sensing Lab, Tahoe National Forest, and USGS # 13-PA-11051700-028. (February).

van de Giesen, N., Steele-Dunne, S.C., Jansen, J., Hoes, O., Hausner, M.B., Tyler, S., Selker, J., 2012. Double-ended calibration of fiber-optic raman spectra distributed temperature sensing data. Sensors 12 (5), 5471–5485. https://doi.org/10.3390/s120505471. (Switzerland).

Veatch, W., Brooks, P.D., Gustafson, J.R., Molotch, N.P., 2009. Quantifying the effects of forest canopy cover on net snow accumulation at a continental, mid-latitude site. Ecohydrology 2 (2), 115–128. https://doi.org/10.1002/eco.45.

Webster, C., Rutter, N., Jonas, T., 2017. Improving representation of canopy temperatures for modeling subcanopy incoming longwave radiation to the snow surface. J. Geophys. Res. Atmos. 122, 9154–9172. https://doi.org/10.1002/2017JD026581.

Wrzesien, M.L., Durand, M.T., Pavelsky, T.M., Howat, I.M., Margulis, S.A., Huning, L.S., 2017. Comparison of methods to estimate snow water equivalent at the mountain range scale: a case study of the California Sierra Nevada. J. Hydrometeorol. 18 (4), 1101–1119. https://doi.org/10.1175/JHM-D-16-0246.1.

Zheng, Z., Kirchner, P.B., Bales, R.C., 2016. Topographic and vegetation effects on snow accumulation in the southern Sierra Nevada: a statistical summary from lidar data. Cryosphere 10 (1), 257–269. https://doi.org/10.5194/tc-10-257-2016.